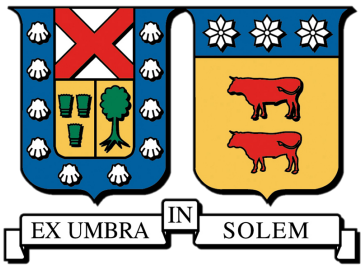

UNIVERSIDAD TÉCNICA FEDERICO SANTA MARÍA

FACULTAD DE CIENCIAS
DEPARTAMENTO DE FÍSICA

CONICAL-HELIX MAGNETIC TEXTURES STABILIZED IN THIN FILMS WITH DIFFERENT KINDS OF DZYALOSHINSKII-MORIYA INTERACTION

Tesis de Grado presesentada por

Matías Nicolás Fernando Cepeda Arancibia

como requisito para optar al grado de

Magíster en Ciencias, Mención Física

Tutor

Prof. Pedro Miguel Landeros Silva

Co-tutor

Dr. David Ignacio Cortés Ortuño

Valparaiso, Chile, 2025

CONSTANCIA DE VALIDACIÓN Y CONFIDENCIALIDAD DE MONOGRAFÍA A REPOSITORIO ACADÉMICO

1.- IDENTIFICACIÓN DEL TRABAJO ACADÉMICO

Tipo de monografía (marcar una opción): ☐ Memoria o trabajo de título; ☒ Tesis de Postgrado;

Título del trabajo: CONICAL-HELIX MAGNETIC TEXTURES STABILIZED IN THIN FILMS WITH DIFFERENT KINDS OF DZYALOSHINSKII-MORIYA INTERACTION

Nombre del candidato(a): Matías Nicolás Fernando Cepeda Arancibia

Carrera / Grado: Magíster en Ciencias, Mención Física

Campus: Casa Central Valparaiso **;** **Departamento**: Física

2.- VALIDACIÓN DEL PROFESOR GUÍA/DIRECTOR DE TESIS

Yo, Pedro Landeros Silva, en mi calidad de profesor(a) guía/director(a) del trabajo académico mencionado anteriormente **DEJO CONSTANCIA** que:

- He revisado esta versión del documento y corresponde a la versión final aprobada del trabajo.
- El trabajo cumple con los requisitos académicos y de formato establecidos por la institución

3.- EVALUACIÓN DE CONFIDENCIALIDAD POR PROPIEDAD INDUSTRIAL

☒ El trabajo **NO contiene información que amerite confidencialidad** y puede ser publicado de inmediato en repositorio con acceso abierto.

☐ El trabajo **CONTIENE** información con potenciales implicancias de propiedad industrial o intelectual y requiere un periodo de confidencialidad (embargo) por:

☐ 6 meses; ☐ 12 meses; ☐ 2 años; ☐ 3 años; ☐ 5 años; ☐ 10 años

Fundamentación de la necesidad de confidencialidad (obligatorio si se solicita embargo):

4.- FIRMAS

Profesor(a) guía o director(a) de memoria o tesis:

Fecha: 30-06-2025 ; **Firma:** _____

Estudiante o Candidato(a):

Fecha: 30-06-2025 ; **Firma:** _____

Este formulario debe ser insertado como página 2 de la memoria o tesis, completado y firmado por estudiante y profesor(a) antes de la entrega en portal PRISMA de Biblioteca USM.

To my father,
who always believed in me.

Acknowledge

The main reason I was able to complete this challenge was the constant support from my family, who always placed their trust in me. I want to emphasize the role of my father and mother; I will be eternally grateful for the unconditional love you have given me and for the trust you placed in allowing me to leave home to study what I am passionate about, even if it means being far away.
My journey through university was never a solitary one; I was fortunate to always be surrounded by wonderful people. For that reason, I want to thank the friends who accompanied me during my time at university. Each of them made this experience more enjoyable, with mutual support and companionship. I especially want to mention Benja, Danilo, Tomi, Felipe, and Joaco.
I must also thank my girlfriend, Kim. Thank you for standing by me during my most difficult moments and for your unwavering support.
I am deeply grateful to my thesis advisor, Professor Pedro Landeros, for his guidance, availability, and patience. I would also express my gratitud to Dr. Rodolfo Gallardo and the Magnetism Group for the fruitful discussions, which were of great importance to the development of this work.
Finally, I thank the Universidad Técnica Federico Santa María for all the tools and opportunities provided throughout my academic formation, as well as the professors, outstanding researchers, whose passion is genuinely transmitted to their students.

Matías Cepeda Arancibia

Introduction

In the last decade, the observation of chiral spin textures in magnetic materials, stabilized by the Dzyaloshinskii-Moriya interaction, has sparked great interest due to their potential applications in spintronics. Those chiral spin textures are presented in different systems, such as ultrathin ferromagnetic films with a specific lack of inversion symmetry in their crystallographic structure. This kind of system spawns a new interaction between spins, called Dzyaloshinskii-Moriya coupling, which differs from the usual interactions since it induces a canting of the spins with a given chirality. It has been reported that in thin films with DM interaction, the magnetization profile follows a conical helix.
This work is focused on finding how the conical-helix spin textures depend on the size of the ultrathin film, considering different classes of symmetries for the Dzyaloshinskii-Moriya interaction, such as the T (bulk), C_{nv} (interfacial), D_{2d}, anisotropic, D_n, and C_n symmetry classes.
In the first chapter, the formalism to describe the problem is introduced, detailing the continuum energy terms associated with the different interactions of the system. Then in the second chapter a simple model that characterizes the magnetic texture is proposed, and the total energy of the film is minimized, thus obtaining the parameters that characterize it. Subsequently, the variation of these parameters are analyzed as the film size decreases. The process is repeated for different classes of symmetries of the Dzyaloshinskii-Moriya interaction, and the confinement effects are analyzed for each case. Additionally, analytical formulas for the nucleation fields for each symmetry class were obtained.

Contents

Chapter 1

Micromagnetism

The behavior of magnetic materials is primarily characterized by their magnetic moment. This quantity originates from the spin and orbital angular momentum of electrons through the motion of the electric charge within the atoms and the intrinsic spin. Then, based on the response of the magnetic moments when a magnetic field is applied, materials can be classified into several groups [1–3]. One of them includes diamagnetic materials, in which the weak magnetic moments are induced in an orientation antiparallel to an applied magnetic field. These materials do not preserve the magnetic ordering once the external field is removed. This behavior stems from the fact that the atoms in diamagnetic materials do not possess a net magnetic moment because their electrons are fully paired [2].

The next group is paramagnetic materials, where the magnetic moments are weak and align parallel to an applied field due to the torque induced by the field. Like diamagnets, the paramagnetic materials lose their magnetic ordering once the external field is removed. However, unlike diamagnetic materials, the atoms in paramagnets contain unpaired electrons and a net magnetic moment. The lack of magnetic ordering in the absence of a field is because individual magnetic moments are randomly oriented [4].

Interestingly, ferromagnetic materials exhibit strong magnetic moments that tend to align parallel to an applied magnetic field. These materials can retain the magnetic ordering even after removing the applied magnetic field, resulting in spontaneous magnetization. Soft magnetic materials are usually partitioned into regions known as magnetic domains, within which the magnetic moments are uniformly aligned. These domains are responsible for the macroscopic magnetization observed in ferromagnetic materials. In the unmagnetized state, the domains are randomly oriented, resulting in a net magnetization of zero. However, upon application of a magnetic field, the domains align, leading to a net average of the magnetic moment over the volume, well-known as magnetization. Ferromagnetic materials lose their magnetic order when heated above their Curie temperature, at which there is a transition into a paramagnetic state [1].

This thesis focuses on ferromagnetic materials, which exhibit strong magnetic order below their Curie temperature [1]. In ferromagnetic materials, atomic spins interact via the quantum mechanical exchange interaction, favoring alignment in the same direction. The Heisenberg Hamiltonian describes this symmetric exchange coupling. The problem with working this interaction at the microscale, where quantum mechanics accurately models atomic-scale interactions, is that applying quantum theory directly to systems with a large number of atoms is computationally impractical. To address this challenge, a

micromagnetic model was developed, which is valid when the characteristic length of the problem is much larger than the lattice constant.

The micromagnetic model is a semiclassical theory that approximates a discrete atomic array as a continuous medium and considers the quantum spins as classical vectors while incorporating essential quantum mechanical effects, such as the exchange interaction [1]. This theory considers a homogeneous array of identical spins which may have different orientations. Therefore, the discrete distribution of magnetic moments is well approximated by a continuous vector density $\mathbf{M}(\mathbf{r}, t)$, the magnetization. For this thesis, the dynamic effects of the magnetization are not considered, and the static magnetization has a constant norm at low temperatures that can be written in terms of a unit vector $\mathbf{m}(\mathbf{r})$ as

$$\mathbf{M}(\mathbf{r}) = M_\mathrm{s}\mathbf{m}(\mathbf{r}), \tag{1.1}$$

where M_s is the saturation magnetization. The different energy contributions depend on the magnetization. The micromagnetic theory seeks to determine the internal magnetization structure that minimizes the total free energy. Getting this goal can be challenging since the dipolar coupling is nonlinear and nonlocal. Therefore, a method employed in this thesis involves assuming a magnetization texture with defined parameters based on reports of similar systems, calculating the total free energy, and minimizing it concerning the parameters characterizing the texture. The subsequent section introduces the different energy contributions whose competence is relevant to the internal magnetization texture.

1.1 Free Energy

1.1.1 Zeeman interaction

When an external magnetic field $\mathbf{H}_\mathrm{ze}$ is applied to a ferromagnetic medium, its magnetic moments tend to align parallel to the field. This coupling is described by the Zeeman energy, which, according to micromagnetic theory, is expressed as:

$$E_\mathrm{ze} = -\mu_0 \int_V \mathbf{M} \cdot \mathbf{H}_\mathrm{ze}\, dV, \tag{1.2}$$

with μ_0 being the vacuum permeability. Equation 1.2 shows that the energy minimum is achieved when the magnetization is aligned with the field.

1.1.2 Dipolar coupling

The dipolar coupling energy describes the classical magnetic dipole-dipole interaction in a magnetic material. For a continuous magnetization $\mathbf{M} = M_\mathrm{s}\mathbf{m}$ and in the absence of electric currents, Maxwell's equations reduce to

$$\nabla \cdot \mathbf{B} = 0, \tag{1.3}$$

$$\nabla \times \mathbf{H}_\mathrm{dip} = 0, \tag{1.4}$$

where the magnetic field $\mathbf{B}$ can be written in terms of the dipolar magnetic field $\mathbf{H}_\mathrm{dip}$ and the magnetization $\mathbf{M}$

$$\mathbf{B} = \mu_0 \left(\mathbf{H}_\mathrm{dip} + \mathbf{M}\right). \tag{1.5}$$

According to 1.4, a magnetic scalar potential U can be defined through $\mathbf{H}_\mathrm{dip} = -\nabla U$, which transforms magnetic Gauss's law into a Poisson equation for U. Then, substituting

equation 1.5 in equation 1.3 and writing the magnetic field in terms of the magnetic scalar potential,

$$-\nabla \cdot (\nabla U) + \nabla \cdot \mathbf{M} = 0, \tag{1.6}$$

which is solved in the whole space $\mathbb{R}^3$. Then, the magnetic scalar potential inside and outside of the magnetic material can be written

$$\nabla^2 U_{\text{in}} = \nabla \cdot \mathbf{M} \tag{1.7}$$

$$\nabla^2 U_{\text{out}} = 0. \tag{1.8}$$

This set of differential equations must be solved together with the appropriate boundary conditions for the magnetic scalar potential:

$$U_{\text{in}} = U_{\text{out}}, \tag{1.9}$$

$$\frac{\partial U_{\text{in}}}{\partial n} - \frac{\partial U_{\text{out}}}{\partial n} = \mathbf{M} \cdot \hat{\mathbf{n}}. \tag{1.10}$$

with $\hat{\mathbf{n}}$ the normal vector to the surface. Furthermore, to ensure a physically meaningful and unique solution, the magnetic scalar potential must tend to zero at infinity.

Once the magnetic scalar potential has been obtained, the dipolar field $\mathbf{H}_{\text{dip}}$ can be calculated, and the dipolar coupling energy is expressed as [1, 2]

$$E_{\text{dip}} = -\frac{\mu_0}{2} \int_V \mathbf{M} \cdot \mathbf{H}_{\text{dip}} \, dV. \tag{1.11}$$

Unlike the other energies, this interaction is nonlocal due to the long-range nature of the magnetostatic field raised by the dipoles, which can cause the emergence of chiral effects [5, 6]. In some cases, such as ultrathin films, the energy due to dipolar coupling may be treated as an effective local uniaxial anisotropy [7, 8], although it can not capture the nonlocal nature of the dipolar coupling. Therefore, the complete form of the dipolar coupling is used in this thesis.

1.1.3 Anisotropy energy

The anisotropy energy describes the preferential alignment of the magnetization along specific axes, referred to as easy axes. This energy arises from the spin-orbit coupling, where electron orbits are tied to the crystallographic structure, and their interaction with spins causes the latter to orient along well-defined crystallographic directions [1, 2]. The associated energy density w is typically expressed using phenomenological models involving power series expansions of the magnetization components that account for the crystal symmetry [9]. The coefficients in these expansions are determined experimentally. There are different kinds of anisotropy energy, with the simplest case being uniaxial magnetic anisotropy. This type of anisotropy is present, for instance, in hexagonal crystals [9, 10], and its energy expression depends only on a single parameter: the angle θ between the c-axis and the direction of magnetization. Since the energy is symmetric with respect to the ab-plane, odd powers of $\cos\theta$ are excluded from the power series expansion. The first two terms of this expansion are given by [9]:

$$w_{\text{u}} = -K_1 \cos^2\theta + K_2 \cos^4\theta, \tag{1.12}$$

where the coefficients K_1 and K_2 depends on the temperature. Higher-order terms are usually negligible.

Throughout this thesis, the kind of anisotropy that will be considered is the superficial anisotropy. From a phenomenological point of view, any surface energy term should reflect the tendency of the normal magnetization at the surface to be either parallel or perpendicular to the surface. In a thin film, the anisotropy energy term has an easy axis either parallel or perpendicular to the film plane [11]. A first-order approximation for the surface anisotropy energy term can be expressed as:

$$E_{\text{an}} = -\frac{1}{2}K_{\text{s}}\int(\mathbf{m}\cdot\hat{\mathbf{n}})^2 dS, \tag{1.13}$$

where the integration is performed over the surface of the ferromagnet, $\mathbf{z}$ is a unit vector normal to the film's surface, and K_{s} is the surface anisotropy constant. In an ultrathin film, this energy term can be averaged over the volume, where $K_{\perp} = K_{\text{s}}/d$ represents the surface anisotropy constant normalized by the film thickness d. The resulting volume-averaged surface anisotropy energy is then given by

$$E_{\text{an}} = -\frac{K_{\perp}}{2}\int_V(\mathbf{m}\cdot\hat{\mathbf{z}})^2 dV. \tag{1.14}$$

For $K_{\perp} > 0$ the superficial anisotropy energy favors the alignment of the normal magnetization perpendicular to the film, contrary to the dipolar coupling, which favors the in-plane spin alignment. This competition is encapsulated in the anisotropy/dipolar quality factor $Q = 2K_{\perp}/\mu_0 M_s^2$.

1.1.4 Exchange coupling

The symmetric exchange coupling describes how magnetic moments interact with their neighbors. This interaction has a quantum origin and has no classical analog. The exchange interaction is isotropic concerning the magnetization rotation in the lattice, as it only aligns parallel or antiparallel the neighboring spins without a given preferential orientation. It is the strongest coupling and is responsible for the existence of ferromagnetism and antiferromagnetism. However, it is a short-range interaction that only couples the nearest-neighbor (n.n.) spins. In a discrete spin model the symmetric part of this energy is given by the Heisenberg Hamiltonian:

$$\mathcal{H}_{\text{ex}} = -\sum_{i,j} J_{ij}\mathbf{S}_i\cdot\mathbf{S}_j, \tag{1.15}$$

where $\mathbf{S}_i$, $\mathbf{S}_j$ are the spin operators of sites i and j that are approximately equal, and J_{ij} is the exchange integral, which decays quickly with distance and it is consider zero after a cutoff distance between spins, taking a constant value J for isotropic materials. The exchange integral is positive for parallel alignment or negative for antiparallel alignment. Assuming a homogeneous material and the micromagnetic limit, the exchange energy can be written as:

$$\mathcal{H}_{\text{ex}} = -JS^2\sum_{\text{n.n.}}\cos\phi_{ij}. \tag{1.16}$$

where S is the average spin, Small angles between neighboring spins are expected since this strong interaction acts only to the nearest neighbors. Thus, the cosine function can be expanded as:

$$\mathcal{H}_{\text{ex}} \approx -JS^2\sum_{\text{n.n}}\left(1-\frac{\phi_{ij}^2}{2}\right). \tag{1.17}$$

Here, the sum in index i runs over the entire sample, while the sum in j runs over the n.n. of site i. The first term corresponds to the constant energy of the saturated state [1]. In the continuum approximation, the exchange energy density is given by:

$$\mathcal{H}_{\text{ex}} = A \int_V \left[(\nabla m_x)^2 + (\nabla m_y)^2 + (\nabla m_z)^2 \right] \, dV, \tag{1.18}$$

where $A = JS^2c/a$ is the exchange stiffness constant, with a the side of the cell and c the coordination number.

1.2 Kinds of Dzyaloshinskii-Moriya interactions

The properties of so called chiral magnets are strongly influenced by the Dzyaloshinskii-Moriya interaction (DMI). In seminal work [12], Dzyaloshinskii studied weak ferromagnetism, a phenomenon that commonly appears in antiferromagnets due to anisotropic exchange interactions. To describe this behavior, he phenomenologically introduced the asymmetric exchange interaction (AEI) using symmetry arguments, pointing out that magnetic crystals with low symmetry and spin-orbit coupling give rise to AEI. Shortly after, Moriya provided a microscopic derivation of AEI [13] using the theory of superexchange interactions proposed by Anderson [14]. Moreover, Dzyaloshinskii demonstrated that for noncentrosymmetric magnetic crystals, this interaction stabilizes long-period spatially modulated structures with a fixed sense of rotation, i.e. with a chirality, of the total spin vector at each site [15]. The discrete Hamiltonian for DMI is described as:

$$\mathcal{H}_{\text{dm}} = \mathbf{D}_{ij} \cdot (\mathbf{S}_i \times \mathbf{S}_j) \, . \tag{1.19}$$

where $\mathbf{S}_i$, $\mathbf{S}_j$ are neighboring spin vectors, and $\mathbf{D}_{ij}$ is the Dzyaloshinskii-Moriya vector, which depends on the symmetry-breaking mechanism that activates the DMI. This energy is minimized when the adjacent spin vectors are orthogonal. In the micromagnetic limit, the total energy is

$$E_{\text{dm}} = \int_V w_{\text{dm}} \, dV, \tag{1.20}$$

where the energy density w_{dm} changes according to the crystal symmetry, and it is described as a combination of first-order spatial derivatives of the magnetization, known as Lifshitz invariants (LIs) [16–18]:

$$\mathcal{L}_{ij}^{k} = M_i \left(\frac{\partial M_j}{x_k} \right) - M_j \left(\frac{\partial M_i}{x_k} \right) . \tag{1.21}$$

There are different kinds of DMI, depending on the symmetry of the crystal. Bogdanov et al. [16] proposed different types of DMI belonging to a group of known crystallographic classes. The most common symmetry studied is the tetragonal point group T in noncentrosymmetric bulk B20 cubic crystals, which is known as bulk DMI [19]. This symmetry is present, for instance, in MnSi [20–22], FeGe [23–25], $Fe_{1-x}Co_xSi$ [26, 27] and other cubir magnetic compounds [19]. Its energy density is mathematically described as [17]:

$$H_{\text{dm}}^{T} = \frac{D}{\mu_0 M_{\text{s}}^2} \left(\mathcal{L}_{yx}^{z} + \mathcal{L}_{xz}^{y} + \mathcal{L}_{zy}^{x} \right) , \tag{1.22}$$

where D is the strength of the DM coupling measured in J/m^2.

Another commonly studied symmetry is the C_{nv} point group found at interfaces of a ferromagnet and a heavy metal, which is known as interfacial DMI [28–30]. Here, the inversion symmetry breaking occurs at the interface (z-axis) and the energy density is described as:

$$H_{\mathrm{dm}}^{C_{nv}} = \frac{D}{\mu_0 M_{\mathrm{s}}^2} \left(\mathcal{L}_{xz}^{x} + \mathcal{L}_{yz}^{y} \right). \tag{1.23}$$

This work also considers more exotic kinds of symmetries besides the usual T and C_{nv}, such as the D_{2d} symmetry and the anisotropic DMI, whose energy density read:

$$H_{\mathrm{dm}}^{D_{2d}} = \frac{D}{\mu_0 M_{\mathrm{s}}^2} \left(\mathcal{L}_{xz}^{y} + \mathcal{L}_{yz}^{x} \right), \tag{1.24}$$

$$H_{\mathrm{dm}}^{\mathrm{an}} = \frac{D}{\mu_0 M_{\mathrm{s}}^2} \left(\mathcal{L}_{zx}^{x} - \mathcal{L}_{zy}^{y} \right). \tag{1.25}$$

The anisotropic DMI, introduced by Jena et al. [31], emerges in Heusler compounds with a D_{2d} symmetry due to the layered nature of the structure where Pt atoms break inversion symmetry of a magnetic Mn layer differently along the [100] and [010] crystallographic orientations. Finally, crystallographic point groups D_n and C_n, are formed by the combination of two DM terms following the formalism established in [16].

$$H_{\mathrm{dm}}^{D_n} = \frac{D_1}{\mu_0 M_{\mathrm{s}}^2} \left(\mathcal{L}_{xz}^{y} - \mathcal{L}_{yz}^{x} \right) + \frac{D_2}{\mu_0 M_{\mathrm{s}}^2} \left(\mathcal{L}_{xy}^{z} \right) \tag{1.26}$$

$$H_{\mathrm{dm}}^{C_n} = \frac{D_1}{\mu_0 M_{\mathrm{s}}^2} \left(\mathcal{L}_{xz}^{x} + \mathcal{L}_{yz}^{y} \right) + \frac{D_2}{\mu_0 M_{\mathrm{s}}^2} \left(\mathcal{L}_{xz}^{y} - \mathcal{L}_{yz}^{x} \right). \tag{1.27}$$

The classification of DMI according to crystallographic classes arises from the symmetry of the underlying lattice or interface [18]. The specific combination of Lifshitz invariants allowed by symmetry reveals a rich variety of chiral interactions that determine the orientation, stability, and periodicity of magnetic textures in thin films. While the bulk and interfacial DMIs have been widely studied, more exotic symmetry classes such as D_{2d}, anisotropic, D_n, and C_n have received less attention [16], particularly in confined geometries. In this work, we aim to systematically compare the behavior of conical-helix textures stabilized by each of these symmetry classes.

1.3 Conical-Helix magnetic textures

In a ferromagnetic material, the competition among symmetric exchange, Dzyaloshinskii-Moriya, magnetic anisotropy, dipolar, and Zeeman interactions gives rise to a ground state with a noncollinear alignment of the magnetic moments, known as a *magnetic texture* [32]. Only a limited number of inhomogeneous textures are energetically stable. In ultrathin films, the most prominent magnetic textures are stripe domains, Bloch and Néel domain walls [3], as well as skyrmion arrays [20, 33–35] and spin spiral structures [36–38].

Dzyaloshinskii started with the study of chiral magnetic textures, demonstrating that asymmetric exchange interaction can stabilize spatially modulated structures with a fixed rotation sense of the magnetization [12, 15]. Shortly after, Moriya developed a microscopic derivation of AEI. Following their pioneering work, chiral textures have been investigated theoretically and experimentally in different kinds of magnetic crystals. Ishikawa *et al.* [39] and Motoya *et al.* [40] conducted high-resolution neutron diffraction and nuclear magnetic resonance (NMR) studies on MnSi. Both studies concluded that MnSi exhibits a helical

spin structure, with a magnetization process interpreted as due to the helical-conical-ferromagnetic phase transitions [40, 41]. The high-resolution neutron diffraction data confirmed the helical order, while NMR measurements demonstrated that this structure persists even without an external magnetic field. A few years later, Bak and Jensen followed the previously mentioned works, demonstrating that the helical structures observed in MnSi and FeGe are caused by the Dzyaloshinskii-Moriya interaction [42]. Following this, Moriya and Miyadai conducted studies on $Cr_{1/4}NbS_3$, showing that long-period helical spin textures emerge at low temperatures in otherwise ferromagnetic crystals due to AEI [43]. Ishimoto *et al.* [44], determined the field dependence of a long-period helical spin texture in $Fe_{0.8}Co_{0.2}Si$ by long-wavelength polarized-neutron diffraction experiments. They showed that clockwise and counterclockwise helices were observed in any direction when the sample was cooled without a bias magnetic field. Once the magnetic field was applied and removed, a single clockwise helix stabilized parallel to the field direction.

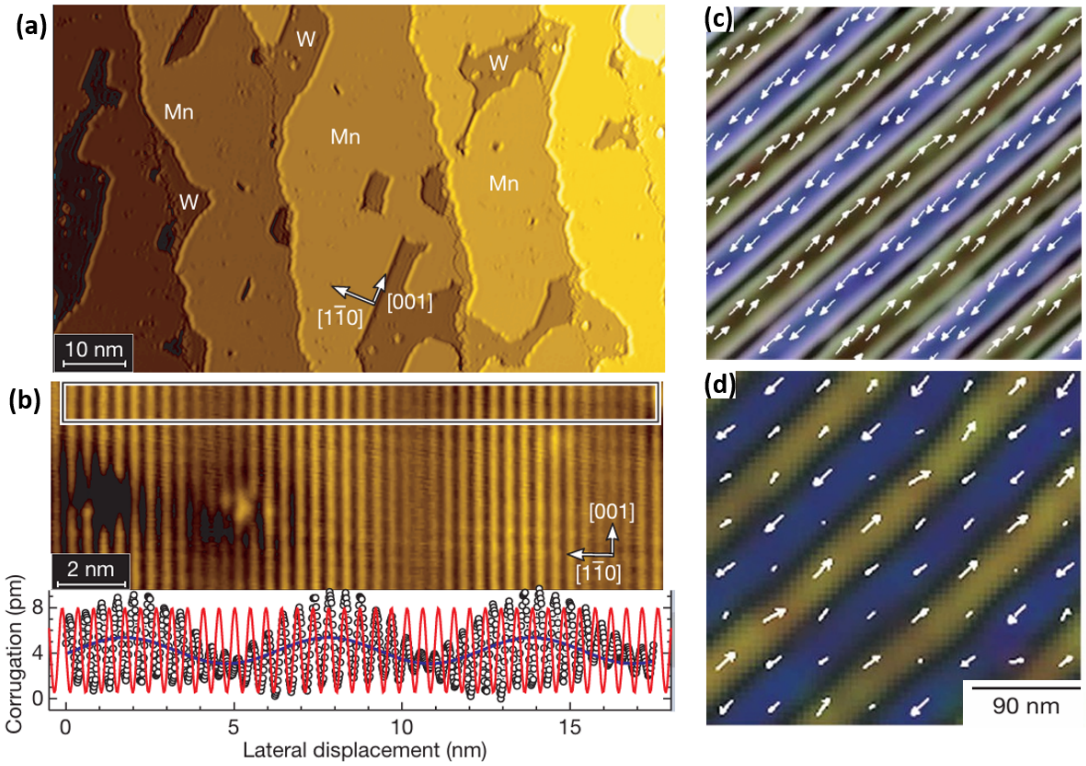

Figure 1.1: (**a**) Topography of atomic layers of Mn grown on a W(001) substrate obtained from spin-polarized scanning tunneling microscopy (SP-STM). (**b**) The upper panel shows a high-resolution constant-current image of the Mn layer taken with a Cr-coated tip, while the lower panel illustrates an antiferromagnetic magnetic corrugation along the monolayer with a nominal periodicity of 0.448 nm and a longer-wavelength spin-spiral modulation with 6 nm period. Adapted from Bode et al. [45]. Panel (**c**) illustrates a helical texture obtained with Monte Carlo simulations, while panel (**d**) depicts a real-space image of a 90 nm period spin helical texture in the noncentrosymmetric helimagnet $Fe_{0.5}Co_{0.5}Si$ belonging to the T symmetry class. Adapted from Yu et al. [46]

.

Fert [28] and Bode *et al.* [45] establish that the antisymmetric exchange (or DMI) is an essential interaction in low-dimensional systems that lack inversion symmetry, such as thin films, interfaces, clusters, and atomic wires. They used spin-polarized scanning tun-

neling microscopy (SP-STM) to map chiral helical textures in layers of Mn grown on a W(001) substrate. Figure 1.1(a) shows the topography of 0.77 atomic layers of Mn grown on a W(110) substrate, while Fig. 1.1(b) shows a high spatial resolution constant-current image measurement on the atomically flat Mn layer taken with a Cr-coated tip (upper panel) [45]. The line section in Figure 1.1(b), lower panel, shows the modulation of the magnetic amplitude, which adjusts the experimental data with a simple sine function (red line) that reveals a phase shift of π between adjacent antinodes.

1.3.1 Spin Waves

The low-energy excitations in magnetic materials are known as spin waves and represent the collective motion of the magnetization [47–52]. These spin waves are usually reciprocal but if spatial symmetry is broken, they can behave nonreciprocally and travel in opposite directions with different wavelengths [29, 30]. In 2010, Zakeri *et al.* [53] experimentally measured, for the first time, the influence of the Dzyaloshinskii-Moriya interaction on the spin-wave dispersion in a Fe double layer grown on a W(100) substrate. They used spin-polarized electron energy loss (SPEELS) measurements to demonstrate the asymmetry of the spin-wave dispersion due to the interfacial DMI. Such an important discovery followed early theoretical works [54–57] predicting the same behavior. These works estimate the dispersion relation in the presence of bulk and interfacial DMI in a uniformly magnetized film [29, 30]. For fields lower than a critical field, one can expect the formation of conical-helical periodic textures [58, 59]. Interestingly, periodic magnetic textures produce periodic magnetic potentials that cause the magnonic crystal-like behavior of spin waves in a film with DMI [60–63]. These elementary excitations, called helimagnons, exhibit a reconfigurable magnon band structure since, by increasing the applied field beyond saturation, the magnetization evolves from a conical-helix state to a uniformly magnetized state, which has an entirely different dispersion. Therefore, detailed knowledge of the conical-helix textures may help in calculating analytically the spin-wave band structure of helimagnons, which has only been obtained numerically [64].

1.4 Nucleation fields

The concept of the nucleation field refers to the external magnetic field strength at which an initial saturated state of a magnetic system becomes unstable, thereby allowing the onset of a new magnetization configuration [1]. The nucleation field is a valuable quantity that allows for understanding the emergence of magnetic textures. As mentioned earlier, within the framework of micromagnetic theory, it is possible to assume a model for the magnetization that characterizes a particular texture. For each of these textures, a corresponding nucleation field can be computed if the system initially resides in a saturated state under a high external field. Then, as the field is progressively reduced, reaching a critical value, the saturated state is no longer an energy minimum, and a magnetic texture nucleates. The texture associated with the highest nucleation field is the one that first becomes accessible as the field decreases, and therefore, it determines the actual reversal path.

As already mentioned, the magnetic state of the system depends on the external magnetic field history, but it can also rely on other parameters. Then, a phase diagram showing the different magnetic states of the system, according to the problem conditions, can be

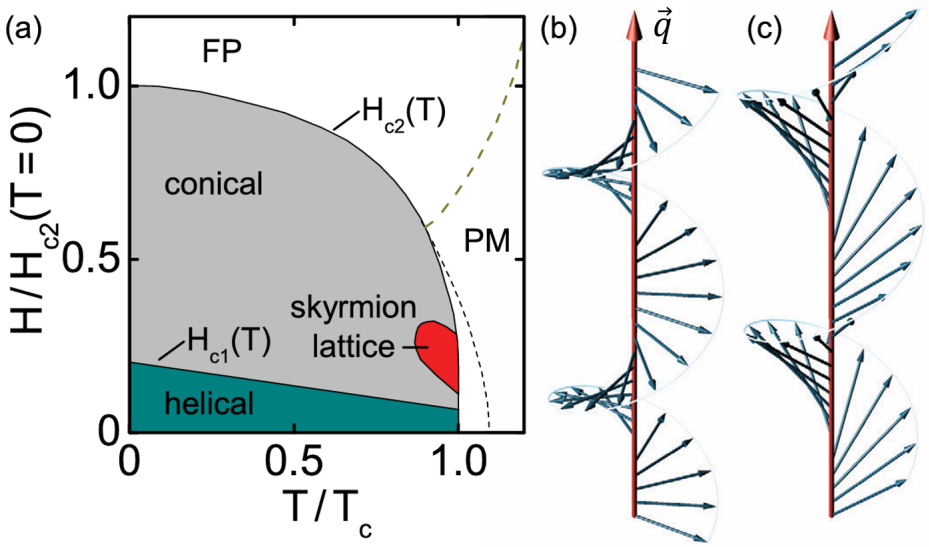

Figure 1.2: (**a**) Illustration of a typical magnetic field/temperature phase diagram of a noncentrosymmetric helimagnet defining the critical (nucleation) field H_{c2}, which gives the transition between the field polarized state (FP), obtained with $\theta = 0$, and the conical states ($0 < \theta < \pi/2$). The other critical field H_{c1} gives the transition between the conical and helical ($\theta \approx \pi/2$) states, which are illustrated in (**b**) and (**c**). Adapted from Garst et al. [64].

constructed. Figure 1.2 depicts a phase diagram for cubic chiral helimagnets, where the external magnetic field and temperature determine the magnetic phases of the system. As expected, for temperatures above the Curie temperature T_c, the system transitions into the paramagnetic (PM) state. Below this critical temperature, when the external magnetic field exceeds a critical field $H_{c2}(T)$, the conical phase becomes unstable, and the system enters the field-polarized (FP) state, where the magnetization aligns uniformly with the external field.

Chapter 2

Conical-helix magnetic textures stabilized with different kinds of Dzyaloshinkii-Moriya interactions

In this chapter, an analytical model is formulated for a conical-helix magnetic texture in ferromagnetic thin films with different crystal symmetry classes, which implies different kinds of DM interactions. A parameterized model for the magnetization is assumed, allowing to describe and minimize the energy of the system. As a result, parameters, such as the pitch vector of the helices and the critical field for the nucleation of the helices, can be determined. The theoretical results are compared with micromagnetic simulations [65].

Section 2.1 introduce the model and its main parameters, section 2.2.1 calculates the Dzyaloshinskii-Moriya (DM) interaction of interfacial type as an illustration. Section 2.4 the pitch vector of the helices that minimized the energy of the magnetic system is obtained, considering its direction and magnitude. After that, in section 2.5 the analytical expression for the nucleation fields for every symmetry class are derived. Finally, in section 2.6 the boundary conditions of the finite film are calculated.

2.1 Conical-helix magnetization structure

In the following sections of this thesis, we adopt a methodology to describe the magnetization texture present in ultrathin magnetic films. The method consists in assuming a magnetization configuration, $\mathbf{M}(\mathbf{r})$, and studying its behavior through the parameters that characterize the texture. Moreover, the magnetization texture is compared with other possible configurations to determine which one is physically meaningful, based on the analysis of the nucleation field, as will be discussed later. A second more general method, treats the total micromagnetic energy as a functional $E[\mathbf{m}]$ and minimizes it using a variational approach. This leads to the Brown equations [1], from which the effective field and the natural boundary conditions can be obtained. These boundary conditions include both symmetric and antisymmetric exchange terms (see Table 2.1).

In order to solve the variational problem analytically, the dipolar interaction is often approximated by an effective uniaxial anisotropy with a hard axis perpendicular to the film plane. Due to the complexity of solving the full micromagnetic equations in more than one spatial dimension, a further simplification typically involves reducing the problem to a one-dimensional model, enabling analytical helical solutions, as shown in [66]. However,

we do not adopt this approach here, as our goal is to retain the full non-local character of the dipolar interaction. As shown in [42], a conical-helix spin structure can be stabilized in the presence of DMI, allowing the introduction of a conical-helix magnetization structure model. This model enables the study of its parameters following the work of Rios *et al.* [58] and Garst *et al.* [64]. Considering a film with its normal axis along the z-axis, and an applied magnetic field along the y-axis, see Fig. 2.1, the conical-helix magnetization is given by [65]:

$$\mathbf{m}(\mathbf{r}) = \begin{pmatrix} \sin(\mathbf{q}\cdot\mathbf{r}+\psi)\sin\theta \\ \cos\theta \\ \cos(\mathbf{q}\cdot\mathbf{r}+\psi)\sin\theta \end{pmatrix}. \tag{2.1}$$

The conical-helix is characterized by the following parameters: the cone angle θ; the pitch vector $\mathbf{q} = q(\sin\varphi_q, \cos\varphi_q, 0)$ at an angle φ_q with respect to the applied field $\mathbf{H}$; and the nucleation field $\mathbf{H}_n$, which marks the onset of the conical-helix formation. Furthermore, ψ is a phase angle that depends on the competition between the dipolar demagnetization and perpendicular anisotropy fields, see section 2.4. The magnetic material is confined to a finite square geometry with position vector $\mathbf{r}$ and spatial coordinates restricted to $x \in [-L_x/2, L_x/2]$, $y \in [-L_y/2, L_y/2]$, and $z \in [-d/2, d/2]$, where the film thickness is much smaller than its lateral dimensions ($d \ll L_x, L_y$), as seen in Fig. 2.1.

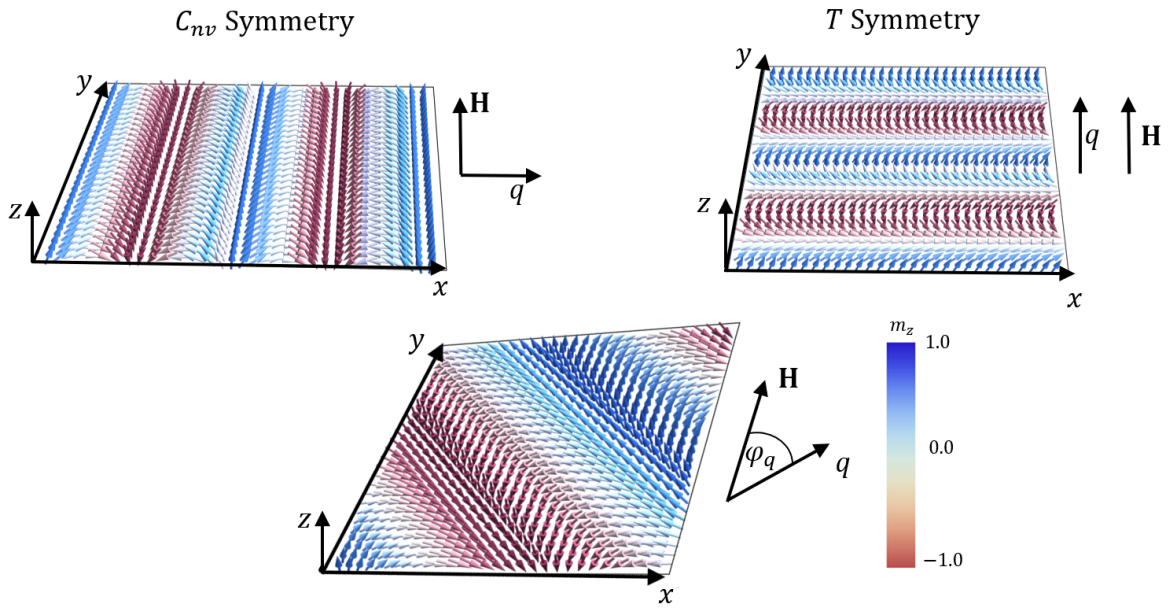

Figure 2.1: Representation of helical magnetic profiles stabilized by the Dzyaloshinskii-Moriya coupling in C_{nv} and T symmetry classes for a cone angle $\theta = \pi/2$. The external field $\mathbf{H}$ is applied along the y-axis, which is then reduced to zero to allow the helix formation. The pitch vector $\mathbf{q}$ points perpendicular (for C_{nv} symmetry) or parallel (for T symmetry) to the applied field, respectively. In the bottom panel, the twisted helix for the C_n symmetry is illustrated. The angle φ_q illustrated in the bottom panel gives the direction between the field direction $\mathbf{H}$ and the helical pitch vector $\mathbf{q}$, and the color code represents the normal magnetization component.

Ríos *et al.* [58] implemented the model described in equation 2.1 to characterize the static properties of a conical-helix magnetization texture in ultrathin films of infinite extension (discarding the phase angle ψ), stabilized by both bulk and interfacial Dzyaloshinskii-Moriya interactions. They demonstrated that the pitch vector of the texture coincides

with the critical wave vector—evaluated at zero frequency—of the spin-wave dispersion relation. Subsequently, in his thesis work, Ríos introduced a phase-shift term into the magnetization model to study the effects of finite film size, discussing the role and impact of this additional phase-shift term. For comparison with the spin-wave dispersion relation, he reverted to the model assuming an infinite film. He kept the study of the magnetic textures stabilized by both bulk and interfacial DMI. In this thesis we exploring other kinds of DMI and studied the parameters that characterize the spin texture in confined films.

2.2 Total energy

The total micromagnetic energy of the system consists of multiple competing interactions, which define the equilibrium magnetization structure. The energies present in the system were introduced in Section 1.1, and section 1.2 of Chapter 1. Then the micromagnetic energy is expressed as:

$$E_{\text{tot}} = E_{\text{ex}} + E_{\text{ze}} + E_{\text{an}} + E_{\text{dip}} + E_{\text{dm}}, \tag{2.2}$$

where E_{ex} is the exchange interaction, E_{ze} is the Zeeman energy due to the external magnetic field, E_{an} is the superficial (perpendicular) anisotropy, E_{dip} is the dipolar coupling, and E_{dm} is the Dzyaloshinskii-Moriya interaction (DMI). The Dzyaloshinskii-Moriya (DM) energy depends on the crystallographic symmetry of the material, and it is expected that the parameters characterizing the conical-helix structure vary depending on the specific form of the DMI employed. For simplicity, a normalized energy expression is used throughout this work, $\varepsilon = E/(\mu_0 M_{\text{s}}^2 V)$, where M_{s} is the spontaneous magnetization, and V the volume of the system. The energy terms are calculated in Appendix A, with the exception of the DM contributions, which are calculated in the following section. Given the total energy:

$$\begin{aligned}
\frac{E}{\mu_0 M_{\text{s}}^2 V} =& \frac{Aq^2}{\mu_0 M_{\text{s}}^2}\sin\theta + \frac{E_{\text{dm}}}{\mu_0 M_{\text{s}}^2 V} - \frac{H\cos\theta}{M_{\text{s}}} \\
&- \frac{K_\perp \sin\theta}{2\mu_0 M_{\text{s}}^2}\left[1 + \text{sinc}(qL_x\cos\varphi_q)\text{sinc}(qL_y\sin\varphi_q)\cos 2\psi\right] \\
&+ \frac{\sin\theta}{4qd}\left[(qd + e^{-qd} - 1)\sin\theta\sin^2\varphi_q(1 - \text{sinc}(qL_x\cos\varphi_q)\text{sinc}(qL_y\sin\varphi_q)\cos 2\psi)\right] \\
&+ \frac{\sin\theta}{4qd}\left[4(qd + e^{-qd} - 1)\cos\theta\sin\psi\sin^2\varphi_q\text{sinc}(qL_x\cos\varphi_q)\text{sinc}(qL_y\sin\varphi_q)\right] \\
&+ \frac{\sin\theta}{4qd}\left[\sin\theta(1 - e^{-qd})(1 + \text{sinc}(qL_x\cos\varphi_q)\text{sinc}(qL_y\sin\varphi_q)\cos 2\psi)\right],
\end{aligned} \tag{2.3}$$

here E_{dm} depend on the crystallographic symmetry.

2.2.1 Interfacial Dzyaloshinskii-Moriya energy (C_{nv} symmetry)

As mentioned above, the DMI changes according to the crystallographic symmetry. In the micromagnetic limit, the energy due to the Dzyaloshinskii-Moriya coupling is calculated as [16]:

$$E_{\text{dm}} = \int w_{\text{dm}}\, \text{d}V, \tag{2.4}$$

where w_{dm} is the energy density. Depending on the crystal symmetry, w_{dm} is expressed as a specific combination of Lifshitz invariants [16–18]. As mentioned in Sec. 1.2, we focus on a specific symmetry to illustrate the calculation of the DM energy. For the C_{nv} symmetry, which corresponds to interfacial DMI [30], the energy density is given by:

$$w_{i-\mathrm{dm}} = \frac{D}{M_{\mathrm{s}}^2}\left(\mathcal{L}_{yz}^{y} + \mathcal{L}_{xz}^{x}\right), \tag{2.5}$$

which, after unraveling the Lifshitz invariants, reads

$$w_{i-\mathrm{dm}} = \frac{D}{\mu_0 M_{\mathrm{s}}^2}\left(M_y\frac{\partial M_z}{\partial y} - M_z\frac{\partial M_y}{\partial y} - M_x\frac{\partial M_z}{\partial x} + M_z\frac{\partial M_x}{\partial x}\right). \tag{2.6}$$

By inserting the conical-helix magnetization model (Eq. 2.1), integrating the energy density within the volume, and then normalizing it by $\mu_0 M_{\mathrm{s}}^2 V$, the DM normalized energy for the C_{nv} symmetry is:

$$\varepsilon_{i-\mathrm{dm}} = -\frac{q_x D}{\mu_0 M_{\mathrm{s}}^2}\sin^2\theta - \frac{q_y D}{2\mu_0 M_{\mathrm{s}}^2}\,\beta(\mathbf{q},\psi,\theta). \tag{2.7}$$

Here, the first term arises from $\mathcal{L}_{yz}^{y}$. The next one arises from $\mathcal{L}_{xz}^{x}$, and depends on

$$\beta(\mathbf{q},\psi,\theta) = \mathrm{sinc}\left(\frac{q_x L_x}{2}\right)\,\mathrm{sinc}\left(\frac{q_y L_y}{2}\right)\sin\psi\sin 2\theta \tag{2.8}$$

where $\mathrm{sinc}(x) = \frac{\sin x}{x}$ is the cardinal sine function. As expected, the DMI energy is proportional to qD and depends on the angle between $\mathbf{q}$ and $\mathbf{H}$, which determines the components of the pitch vector $q_x = q\sin\varphi_q$ and $q_y = q\cos\varphi_q$. This energy term also depends on the phase angle ψ and cone angle θ, as will be discussed in the next section.

2.2.2 Dzyaloshinskii-Moriya energy for C_n symmetry

Following the same procedure used for the C_{nv} symmetry, we now derive the DM energy for the C_n class [67, 68]. Established symmetry classes are interfacial (C_{nv}) and tetragonal (T) or bulk DMI. As detailed in Section 1.2, this symmetry leads to an energy density involving a distinct combination of Lifshitz invariants. Specifically, the energy density w_{dm} under C_n symmetry introduces two independent Dzyaloshinskii-Moriya constants, D_1 and D_2:

$$w_{C_n-\mathrm{dm}} = \frac{D_1}{\mu_0 M_{\mathrm{s}}^2}\left(\mathcal{L}_{xz}^{x} + \mathcal{L}_{yz}^{y}\right) + \frac{D_2}{\mu_0 M_{\mathrm{s}}^2}\left(\mathcal{L}_{xz}^{y} - \mathcal{L}_{yz}^{x}\right). \tag{2.9}$$

We follow the same methodology: insert the conical-helix magnetization model into the DMI energy density, then integrate it over the film volume and normalize the result to obtain the corresponding normalized energy expression.

$$\varepsilon_{C_n-\mathrm{dm}} = -\frac{(D_1 q_x + D_2 q_y)}{\mu_0 M_{\mathrm{s}}^2}\sin^2\theta - \frac{(D_1 q_y + D_2 q_x)}{2\mu_0 M_{\mathrm{s}}^2}\beta(\mathbf{q},\psi,\theta). \tag{2.10}$$

Unlike the other energies, the DMI energy for C_n symmetry depends on both constants D_1 and D_2, which influence the orientation of the magnetization texture, the phase angle ψ, and the nucleation field, as discussed in the next section. Furthermore, the form of the energy under C_n symmetry can be interpreted as a combination of those for the T and C_{nv} classes. This is because, in a thin film regime, the effect of out-of-plane derivatives, (e.g. $\mathcal{L}_{xy}^{z}$), are discarded. Consequently, the DM constant D_1 is the constant associated to the interfacial DMI, C_{nv} symmetry; and the DM constant D_2 is associated to the bulk DMI, T symmetry.

2.2.3 Dzyaloshinskii-Moriya interaction under different symmetry classes

For each crystallographic symmetry class, the calculation procedure is analogous. The third column of Table 2.1 shows the different normalized energies density for each symmetry class (first column), which are obtained from their respective combination of Lifshitz invariants (second column). The similarity of the Lifshitz invariants of the energy density of certain classes is reproduced in the energy term of the conical helix. For instance, classes T and D_{2d} include similar energy densities but with an opposite sign in the term proportional to q_x. From the literature, it can be seen that this negative sign in D_{2d} differentiates the formation of Bloch skyrmions in T class materials from reported anti-skyrmions in D_{2d} [69, 70]. The other symmetry classes preserve the same structure of the conical helix energy density, but interchanging the $q_{x,y}$ components of the pitch vector.

2.3 Micromagnetic Simulations

Micromagnetic simulations were performed using the GPU-accelerated package mumax$^+$ [73], and the solutions were validated using the OOMMF software [74] via the micromagnetic platform Ubermag [75, 76]. The simulated system consists of a square film of size $L \times L$ with a thickness of 1 nm. The discretization cell is defined with a cubic volume of 1 nm^3. Magnetic interactions include symmetric exchange, DMIs (T, C_{nv} and C_n symmetries), dipole-dipole interactions, uniaxial anisotropy along the $z-$axis, and the Zeeman interaction. The magnetic parameters are set as: exchange stiffness A =11.1 pJ/m, uniaxial anisotropy $K_\perp = 0.25$ MJ/m^3 and an external field applied along the $y-$direction. For T and C_{nv} symmetries, the DMI strength was set to $D = 1.5$ mJ/m^2. For the C_n symmetry, which involves two distinct DMI values, one was varied between 0 and 3.0 mJ/m^2, while the other was kept fixed. The same parameters were used in the analytical calculations to enable a direct comparison with the micromagnetic simulations. The simulations are based on a gradual decrease in the magnitude of the external magnetic field, starting from a saturated state at 1 T down to zero, in steps of 5 mT. At every field stage, the energy is minimized using the steepest descent method with a modified Barzilai-Borwein step scheme [73]. This field sweep passes through the critical field at which the conical-helix texture begins to nucleate. At zero field, the texture period is extracted, enabling the calculation of the pitch vector magnitude (q) for each system size L, ranging from 900 nm to 1100 nm in steps of 10 nm. This procedure is carried out for both bulk and interfacial DMI. In the case of the C_n symmetry, the system size is kept fixed, and the critical field is determined. During the nucleation process, and down to zero field, both the pitch vector magnitude (q) and its orientation concerning the external field direction (φ_q) are evaluated. More details about the micromagnetic simulations can be found in the publication associated with this thesis [65].

2.4 Energy Minimization

After introducing the conical-helix magnetization model (Sec. 2.1) and calculating the total energy (Sec. 2.2), the parameters that describe the texture can be determined by minimizing the total normalized energy, which is accomplished in the following sections. In particular, the total energy is minimized according to the angle φ_q, which gives the direction of the pitch vector. The φ_q minimization is carried out numerically since tran-

Symmetry class	$\mu_0 M_s^2\, w_{dm}$	E_{dm}/V	φ_q	B.C. ($\mathbf{G}$)	Refs.
T	$D(\mathcal{L}^z_{yx}+\mathcal{L}^y_{xz}+\mathcal{L}^x_{zy})$	$-q_y D\sin^2\theta+\frac{1}{2}q_x D\,\beta(\mathbf{q},\psi,\theta)$	0	$D\mathbf{m}\times\hat{n}$	[16–18, 29, 64, 71]
$C_{nv},\ n>2$	$D(\mathcal{L}^x_{xz}+\mathcal{L}^y_{yz})$	$-q_x D\sin^2\theta-\frac{1}{2}q_y D\,\beta(\mathbf{q},\psi,\theta)$	$\pi/2$	$D\mathbf{m}\times(\hat{z}\times\hat{n})$	[18, 29, 30]
D_{2d}	$D(\mathcal{L}^y_{xz}+\mathcal{L}^x_{yz})$	$-q_y D\sin^2\theta-\frac{1}{2}q_x D\,\beta(\mathbf{q},\psi,\theta)$	0	$-D(\mathbf{m}\times\mathbf{n}_\parallel)$	[18, 69, 70]
Anisotropic	$D(\mathcal{L}^x_{xz}-\mathcal{L}^y_{yz})$	$-q_x D\sin^2\theta+\frac{1}{2}q_y D\,\beta(\mathbf{q},\psi,\theta)$	$\pi/2$	$D(\mathbf{m}\times\hat{y})(\hat{x}\cdot\hat{n})$ $+D(\mathbf{m}\times\hat{x})(\hat{y}\cdot\hat{n})$	[69, 70, 72]
$D_n,\ n>2$	$D_1(\mathcal{L}^y_{xz}-\mathcal{L}^x_{yz})$ $+D_2(\mathcal{L}^z_{xy})$	$-q_y D_1\sin^2\theta+\frac{1}{2}q_x D_1\,\beta(\mathbf{q},\psi,\theta)$	0	$D_1(\mathbf{m}\times\mathbf{n}_\parallel)$ $+D_2(\mathbf{m}\times\hat{z})(\hat{z}\cdot\hat{n})$	[16, 18]
$C_n, n>2$	$D_1(\mathcal{L}^x_{xz}+\mathcal{L}^y_{yz})$ $+D_2(\mathcal{L}^y_{xz}-\mathcal{L}^x_{yz})$	$-(q_x D_1+q_y D_2)\sin^2\theta$ $-\frac{1}{2}(q_y D_1-q_x D_2)\,\beta(\mathbf{q},\psi,\theta)$	$\arctan\left(\frac{D_1}{D_2}\right)$	$D_1\mathbf{m}\times(\hat{z}\times\hat{n})$ $-D_2(\mathbf{m}\times\mathbf{n}_\parallel)$	[16, 18]

Table 2.1: The table shows, for different symmetry classes, the Dzyaloshinskii-Moriya energy density w_{dm}, the resulting normalized DM energy of the conical-helix ε_{dm}, the pitch-vector angle φ_q, and the DM term $\mathbf{G}$ in the boundary condition $2A\partial\mathbf{m}/\partial n-\mathbf{G}=0$. Here, $\hat{n}$ is the normal to the local surface, where $\mathbf{n}_\parallel=(\hat{n}\cdot\hat{x})\hat{x}+(\hat{n}\cdot\hat{y})\hat{y}$ is the in-plane component. Related references are also shown.

scendental equations arise in the first and second derivatives of the energy. The result of the angle direction are shown in table 2.1. We note that for the T and C_{nv} symmetries, the pitch vector directions coincide with the infinite film case presented by Rios-Venegas et al. [58, 59], which are those that maximize the spin-wave nonreciprocity, $\varphi_q = 0$ for the T symmetry and $\varphi_q = \pi/2$ for the C_{nv} symmetry [29].

For the other symmetries, the direction is distributed between the directions parallel and perpendicular to the applied magnetic field. Based on the results shown in the fourth column in table 2.1, we note that symmetry classes T, D_{2d}, and D_n favor textures aligned parallel to the field. The C_{nv} and Anisotropic symmetries favor textures oriented perpendicular to the magnetic field. In each case, the equilibrium direction of the texture is determined for the angle φ_q that minimizes the first term of the DM energy. This happens because the second term in the DM energy depends on sinc (cardinal sine) functions, which reach a maximum value of one, for arguments equal to zero, and decay for large arguments.
Finally, for the C_n symmetry, the direction of the periodicity of the texture is defined by the competition between two DMI constants D_1 and D_2, as $\varphi_q = \arctan(D_1/D_2)$. In the limit case where D_1 vanishes, it recovers the DM energy for symmetries with the pitch vector parallel to the applied field. In contrast, in the opposite limit $D_2 \to 0$, we recover the DM energy for symmetries with a perpendicular orientation of the pitch vector. Using the fact that $\tan\varphi_q = D_1/D_2$, and defining $\tilde{D} = \sqrt{D_1^2 + D_2^2}$, it can also be noted, by trigonometric arguments, that the pitch vector components are related with the DMI strengths by $q_x/q_y = D_1/D_2$.

2.4.1 Phase angle of the conical helix

Once the direction of the pitch vector is determined, the total energy calculation is facilitated, and the evaluation of other parameters becomes simpler. The first parameter of interest is the phase angle ψ, that in our model provides information about the magnetization of the helix at the center of the film ($\mathbf{r} = 0$). The total energy is derived with respect to ψ, and the critical points are found by solving $\partial\varepsilon/\partial\psi = 0$. For symmetries with the direction of the helical texture parallel to the applied field, that is $\varphi_q = 0$, the extrema condition is:

$$\sin(2\psi)\sin^2\theta\frac{\sin(qL_y)}{qL_y}\left[\frac{K_\perp}{\mu_0 M_s^2} - \frac{1-e^{-qd}}{2qd}\right] = 0. \tag{2.11}$$

On the other hand, symmetries with the direction of the texture perpendicular to the applied field, $\varphi_q = \pi/2$, give:

$$\sin(2\psi)\sin^2\theta\frac{\sin(qL_x)}{qL_x}\left[\frac{K_\perp}{\mu_0 M_s^2} - \frac{1-e^{-qd}}{qd} + \frac{1}{2}\right] = 0. \tag{2.12}$$

For both equations, solutions for the phase angle appear when the bracket is nonzero. Part of the solutions are given by $\sin(2\psi) = 0$, leading to $\psi = n\pi/2$ and then to $\psi = 0$ and $\psi = \pi/2$.

For the C_n symmetry, with two DMI constants, the direction of the texture is determined

by the competition of two DMI constants, and the equation for the extreme points gives:

$$\sin(2\psi)\sin^2\theta\gamma'_x\gamma'_y\left[\frac{K_\perp}{\mu_0 M_s^2}+\frac{(qd+e^{-qd}-1)D_2^2}{4qd\tilde{D}^2}+\frac{(e^{-qd}-1)\tilde{D}^2}{2qdD_2^2}\right]+ \\ \cos\psi\sin(2\theta)\left[\frac{qD_1D_2\gamma_x\gamma_y}{\mu_0 M_s^2\tilde{D}}+\frac{D_1D_2(qd+e^{-qd}-1)\gamma'_x\gamma'_y}{4qd\tilde{D}^2}\right]=0. \tag{2.13}$$

where the auxiliary terms are defined as $\gamma_{x,y}=\frac{1}{2}\text{sinc}\left(\frac{1}{2}L_{x,y}q_{x,y}\right)$ and $\gamma'_{x,y}=\text{sinc}\left(L_{x,y}q_{x,y}\right)$ with $q_x=q\sin\varphi_q$, and $q_y=q\cos\varphi_q$. The first term in Eq. 2.13 depends on the relation between the dipolar and anisotropic energy that appears in the first two equations, while the second term depends on the competition between the DM constants D_1 and D_2. In the limiting cases, $D_1\to 0$, or $D_2\to 0$, the second term vanishes, and the first term recovers the expression obtained in Eq. 2.11 for $D_1\to 0$, and Eq. 2.12 for $D_2\to 0$. The phase angle ψ will have only the extreme value $\psi=\pi/2$, if the second parenthesis is non-zero, or the conical angle is different from $\theta=\pi/2$, which causes the second term not to disappear. In case that the second term vanish, a second extreme value arise $\psi=0$.

Now we check if the critical values are minimum by the condition $\partial^2\varepsilon/\partial\psi^2>0$. For symmetries with parallel and perpendicular helix orientations, the minimum conditions result, respectively, in the following expressions:

$$\cos(2\psi)\sin^2\theta\frac{\sin(qL_y)}{qL_y}\left[\frac{K_\perp}{\mu_0 M_s^2}-\frac{1-e^{-qd}}{2qd}\right]>0, \tag{2.14}$$

and

$$\cos(2\psi)\sin^2\theta\frac{\sin(qL_x)}{qL_x}\left[\frac{K_\perp}{\mu_0 M_s^2}-\frac{1-e^{-qd}}{qd}+\frac{1}{2}\right]>0. \tag{2.15}$$

It can be shown that the exponential function $(1-e^{-qd})/(qd)\to 1$ for realistic values of q and d, that is, $q\approx 0.067$ rad/nm, and $d=1$ nm. Then, using the definition of the anisotropy/dipole quality factor $Q=2K_\perp/\mu_0 M_s^2$, the minimum condition simplifies to:

$$\cos(2\psi)\sin^2\theta\frac{\sin(qL_y)}{qL_y}\left[Q-1\right]>0, \tag{2.16}$$

and

$$\cos(2\psi)\sin^2\theta\frac{\sin(qL_x)}{qL_x}\left[Q-1\right]>0. \tag{2.17}$$

These equations show that the phase angle takes the value $\psi=0$ when the anisotropy energy is greater than the dipolar energy, that is $Q>1$, indicating that the magnetization tends to point out-of-plane. On the other hand, the phase angle takes the value $\psi=\pi/2$ when the anisotropy energy is less than the dipolar energy ($Q<1$), resulting in a tendency to magnetization in the plane. It is worth mentioning that, if the quality factor is close to 1, the model predicts a conical helix that requires very low values of the DMI constant to be stable [58]. Otherwise, if Q is not close to 1, the competition between the anisotropy energy and the dipolar energy is not balanced, and the conical-helix requires larger values of the DMI constant to stabilize. This can lead to an elliptical helix, which is not described by the model and whose influence is more relevant when the DMI strength is low (larger values of D help to stabilize the conical helix). The description of an elliptical helix is out of the scope of the thesis work. When $Q=1$, the dipolar and

anisotropy fields are equilibrated, and the film becomes completely isotropic. Therefore, there is no solution for the phase angle ψ when $Q = 1$ since the magnetization does not prefer to be either parallel or perpendicular to the film's surface.

Finally, for the C_n symmetry, the minimum condition is:

$$\begin{aligned} 2\cos(2\psi)\sin^2\theta\gamma_x'\gamma_y'\left[\frac{K_\perp}{\mu_0 M_s^2}+\frac{(qd+e^{-qd}-1)D_2^2}{4qd\tilde{D}^2}+\frac{(e^{-qd}-1)\tilde{D}^2}{2qdD_2^2}\right]- \\ \sin\psi\sin(2\theta)\left[\frac{qD_1D_2\gamma_x\gamma_y}{\mu_0 M_s^2\tilde{D}}+\frac{D_1D_2(qd+e^{-qd}-1)\gamma_x'\gamma_y'}{4qd\tilde{D}^2}\right]>0. \end{aligned} \tag{2.18}$$

This expression does not yield a straightforward analytical condition due to the interplay of multiple parameters. Nonetheless, it shows that the stability of the solution for ψ depends on a more delicate balance between the anisotropy and dipolar terms, which enter in the first bracket, and the DMI competition, which appears in the second bracket. Furthermore, the DMI constants D_1 and D_2 influence the pitch vector components q_x and q_y, which are present in almost all the terms.

2.4.2 Wavelength of the helix

The following parameter of interest is the pitch vector magnitude q of the helices, which determines the periodicity (or wavelength) of the magnetic texture through the relation $\lambda = 2\pi/q$. Taking the first derivative of the total normalized energy with respect to the pitch vector strength q, for symmetries where the magnetic texture is aligned parallel to the applied field, such as the T class, the following transcendental equation is obtained:

$$\begin{aligned} \frac{2Aq}{\mu_0 M_s^2}-\frac{D}{\mu_0 M_s^2}-\frac{K_\perp\sin(qL_y)\cos(2\psi)}{2\mu_0 M_s^2 qL_y}-\frac{(1-e^{-qd})}{4q^2d}+\frac{e^{-qd}}{4q} \\ +\cos(2\psi)\left(\frac{(1-e^{-qd})\cos(qL_y)}{2q^2d}-\frac{(1-e^{-qd})\sin(qL_y)}{q^3dL_y}+\frac{e^{-qd}\sin(qL_y)}{2q^2L_y}\right)=0. \end{aligned} \tag{2.19}$$

On the other hand, for symmetries with a perpendicular orientation of the helix with respect to the applied field, such as the C_{nv} class, the transcendental equation is:

$$\begin{aligned} \frac{2Aq}{\mu_0 M_s^2}-\frac{D}{\mu_0 M_s^2}-\frac{K\sin(qL_x)\cos(2\psi)}{2\mu_0 M_s^2 qL_x} \\ +\cos(2\psi)\left(\frac{(1-e^{-qd})\cos(qL_x)}{2q^2d}-\frac{(1-e^{-qd})\sin(qL_x)}{q^3dL_x}+\frac{e^{-qd}\sin(qL_x)}{2q^2L_x}\right)=0. \end{aligned} \tag{2.20}$$

It is important to note that, due to the transcendental nature of these equations, stemming from the dipolar and surface anisotropy contributions, an analytical solution for the pitch vector q cannot be obtained. However, the structure of these equations reveals that the pitch vector magnitude depends explicitly on the lateral dimensions of the film (L_x and L_y). In the case of an infinite film, there is no dependence on these lengths due to the intrinsic translational symmetry. In contrast, for a finite film, just the fact of integrating the energy on the volume, without the necessity of considering boundary conditions, introduces a dependence of the equilibrium pitch vector on the sample size, as evidenced by the presence of L_x and L_y in the transcendental equation.

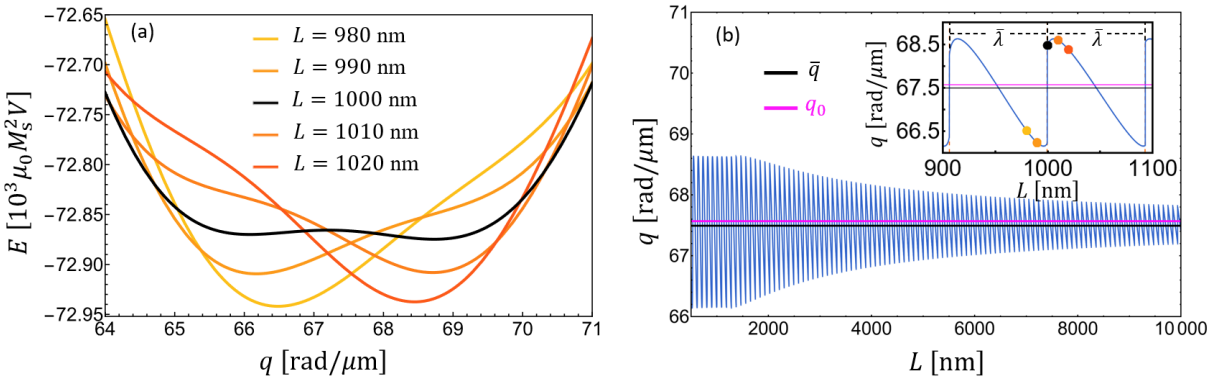

Figure 2.2: In (a), the energy of the conical helix is plotted as a function of the pitch vector magnitude q for different film lengths and fixed DMI strength $D = 1.5$ mJ/m^2. The energy is minimized for a given value of the pitch vector strength except for $L = 1000$ nm (black line), where two minima appear in the energy. In (b), the strength of the pitch vector, q, as a function of the film length is presented. The black line represents the average value of the pitch vector, and the purple line represents $q_0 = D/(2A)$. The inset shows a zoomed-in view of a shorter range of the film length, where the colored dots indicate the values obtained for the corresponding lengths used in (a). Here, $\bar{\lambda}$ is the average period of the oscillation obtained as $\bar{\lambda} = 2\pi/\bar{q}$.

To determine the behavior of the strength of the pitch vector, the total normalized energy is minimized numerically with respect to q for different film lengths L. In Fig. 2.2(a), the normalized total energy for symmetry classes having the orientation of the pitch vector perpendicular to the applied field, are plotted. It can be seen that for most of the values of L, there is a single well-defined energy minimum that changes with the specific value of L, while for $L = 1000$ nm there are two possible values for the pitch vector that minimizes the energy. This indicates that the pitch vector q of the helical structure oscillates and undergoes a discontinuous transition between two values of q. This is shown in the inset of Fig. 2.2(b), where the minimized pitch vector is calculated as a function of L, with the colored dots indicating the values of L plotted in Fig. 2.2(a). In Fig. 2.2(b), the black dashed line represents the average value of the pitch vector magnitude $\bar{q}$. The line shows that, for large film lengths, the q that minimize the energy converge to this average value, which coincides with those obtained for an infinite film, aligning with reported theoretical results [58]. The period of the oscillation is approximately equal to the average wavelength of the conical helix, $\bar{\lambda} = 2\pi/\bar{q}$ (inset of Fig. 2.2), and is inversely proportional to the strength of the DMI. This behavior is observed in symmetries with the orientation of the pitch vector parallel to the magnetic field, $\varphi_q = 0$.

The oscillation of the helical pitch vector with respect to the sample lateral size L is an unexpected result associated with both the dipolar coupling and perpendicular anisotropy in a finite squared film. The wavelength of the texture is calculated as $\lambda(L) = 2\pi/q(L)$, given the wavelength of the helical structure as a function of the film length. This result is depicted in Fig. 2.3(a,b) for two orientations of the helical texture, parallel and perpendicular, where the results of minimizing the total energy are compared with simulations based on mumax$^+$ and OOMMF. Then, for the parameters used here, $K_\perp = 0.25$ MJ/m^3, $D = 1.5$ mJ/m^2, $A = 11.1$ pJ/m; we notice that the discontinuity of the wavelength is about 7 nm.

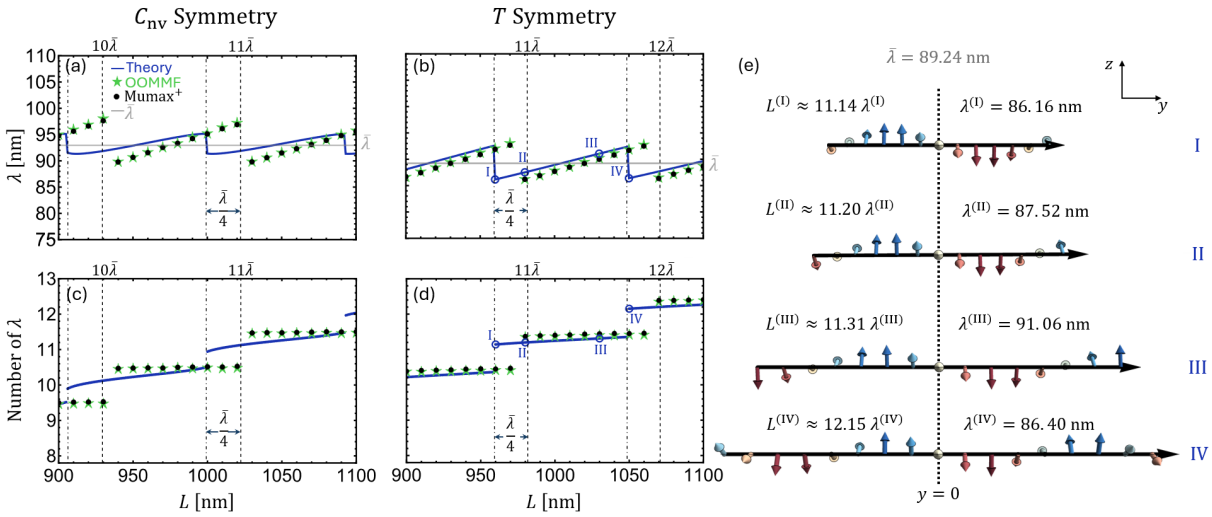

Figure 2.3: Panels (a) and (b) show the wavelength as a function of film length for their respective symmetries, while panels (c) and (d) display the number of wavelengths as a function of film length for the corresponding symmetries. Panel (e) shows a simplified picture of the helix for the T symmetry in cases I-IV marked in panel (b) and (d). In panels (a)-(d), the blue line represents the theoretical results, the black dots indicate the mumax$^+$ simulation results, and the green stars indicate the OOMMF simulation results. Panels (a) and (c) correspond to the C_{nv} symmetry class, with the dashed lines representing integer multiples of $\bar{\lambda}$. Panels (b) and (d) correspond to the T symmetry class.

For a better understanding of the influence of the length in the wavelength of the texture, the number of wavelengths of the helical texture in a film with a length L is plotted in Fig. 2.3(c,d). For both directions of the pitch vector, it is observed that the periodicity of the helical texture adjusts itself to always correspond to approximately a half-integer number of wavelengths. This can be attributed to the dipolar coupling since a half-integer number of wavelengths means that, at opposite edges of the film, the magnetization closed field lines, which reduce the dipolar coupling. As can be seen in Fig. 2.3, micromagnetic simulations also show the jump in q but with a approximately 20 nm shift concerning the theoretical prediction. The difference between the theoretical calculations and the simulations can be attributed to the boundary conditions, as boundary effects are not explicitly considered in the theoretical model. Nonetheless, the model helps us to find the peculiar behavior of the number of wavelengths that can fit in a film of length L.

The periodic steps in q and λ observed when L changes (obtained from theory and simulation) tend to disappear when the perpendicular anisotropy constant increases and approaches the dipolar field. This behavior is particularly noticeable when the anisotropy dipolar quality factor $Q \approx 1$. At this critical value, the model predicts a transition in the phase-angle ψ from $\pi/2$ to 0. The flattening of the periodic steps in Fig. 2.4 can be explained by analyzing the energy terms. When $K_\perp/\mu_0 M_s^2 \approx (1 - e^{-qd})/2qd$ (see equation 2.14), the perpendicular anisotropy and dipolar contributions practically cancel each other. In this case, the system is governed only by the Zeeman, exchange, and Dzyaloshinskii–Moriya interactions. Moreover, the DM term loses its dependence on the film length L because it is evaluated along the direction that minimizes the energy, removing the L-dependent contribution. Therefore, it is worth working with quality factors close to but not exactly $Q = 1$, in order to retain sensitivity to finite-size effects.

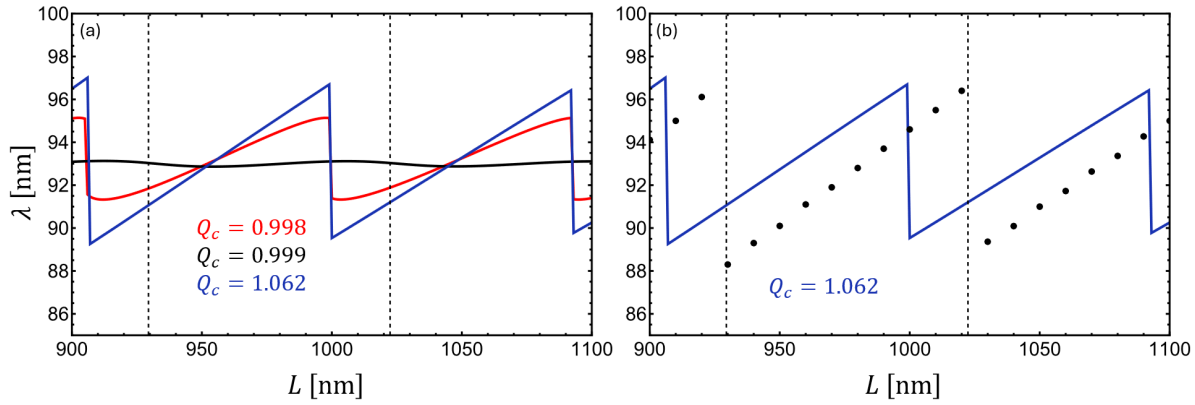

Figure 2.4: Left panel shows the wavelength of the helix as a function of the film length for different anisotropy constant: $K_\perp = 0.25$ mJ/m^3 (red line), $K_\perp = 0.254$ mJ/m^3 (black line), and $K_\perp = 0.27$ mJ/m^3 (blue line), corresponding to $Q = 0.998$, $Q = 0.999$, and $Q = 1.062$, respectively. The right panel shows the comparison between theoretical results and OOMMF simulations for $K_\perp = 0.27$ mJ/m^3.

2.5 Nucleation Field

The nucleation field, H_n, is defined as the value of the external magnetic field at which the saturated state becomes unstable. For applied fields greater than H_n, the film is saturated, i.e., the conical angle is $\theta = 0$, and $\mathbf{m} = \hat{y}$. Then, when the applied field is reduced below H_n, a nontrivial magnetization texture arises, and the conical-helix solution θ_q appears. This solution is obtained by solving the condition $\partial\varepsilon/\partial\theta = 0$. The extreme values of the conical angles are well-defined for symmetries with the texture parallel and perpendicular to the applied field. For symmetries with parallel direction of the pitch vector with respect to the applied field, the extreme values are given by:

$$\sin\theta\left[\frac{H}{M_\mathrm{s}} + \cos\theta\left(\frac{2Aq^2}{\mu_0 M_\mathrm{s}^2} - \frac{2Dq}{\mu_0 M_\mathrm{s}^2} + \left(\frac{1-e^{-qd}}{2qd} - \frac{K_\perp}{\mu_0 M_\mathrm{s}^2}\right)\left(1+\mathrm{sinc}(qL_y)\cos 2\psi\right)\right)\right] = 0, \tag{2.21}$$

while, for perpendicular direction of the pitch vector with respect to the applied field, is given by:

$$\begin{aligned}\sin\theta\Bigg[\frac{H}{M_\mathrm{s}} + \cos\theta\Bigg(&\frac{2Aq^2}{\mu_0 M_\mathrm{s}^2} - \frac{2Dq}{\mu_0 M_\mathrm{s}^2} - \frac{K_\perp}{\mu_0 M_\mathrm{s}^2}\left(1+\mathrm{sinc}(qL_x)\cos 2\psi\right)\\ &+ \frac{1-2e^{-qd}-2qd}{2qd}\mathrm{sinc}(qL_x)\cos 2\psi + \frac{1}{2}\Bigg)\Bigg] = 0.\end{aligned} \tag{2.22}$$

These equations admit three solutions for θ: the homogeneous states $\theta = 0$ and $\theta = \pi$, and the intermediate conical angle θ_q when the bracket vanishes. The solution θ_q for symmetry classes with an helical texture parallel to the applied field is:

$$\theta_q = \cos^{-1}\left(\frac{H/M_\mathrm{s}}{\frac{2q(D-Aq)}{\mu_0 M_\mathrm{s}^2} - \left(\frac{1-e^{-qd}}{2qd} - \frac{K_\perp}{\mu_0 M_\mathrm{s}^2}\right)\left(1+\mathrm{sinc}(qL_y)\cos 2\psi\right)}\right), \tag{2.23}$$

and for symmetry classes with an helical texture perpendicular to the applied field is:

$$\theta_q = \cos^{-1}\left(\frac{H/M_\mathrm{s}}{\frac{2q(D-Aq)}{\mu_0 M_\mathrm{s}^2}+\frac{K_\perp}{\mu_0 M_\mathrm{s}^2}[1+\mathrm{sinc}(qL_y)\cos 2\psi]-\mathrm{sinc}(qL_x)\cos 2\psi\left(\frac{e^{-qd}-1}{qd}+\frac{1}{2}\right)+\frac{1}{2}}\right). \tag{2.24}$$

For both directions, the conical angle θ_q depends on q, L, the external field, and the parameters of the magnetic material. For symmetry C_n, an expression for the critical values cannot be obtained analytically. We know that the saturated state is a minimum when the field is above than an applied field H_n and the condition of minimum, $\partial^2\varepsilon/\partial\theta^2|_{\theta=0} > 0$, is fulfilled. Then, to find the nucleation field, we look in the condition minimum to the critical case when the second derivative is no longer positive, and the second derivative must be zero, $\partial^2\varepsilon/\partial\theta^2|_{\theta=0} = 0$. With this new condition, the nucleation field for symmetries with parallel direction with respect to the applied field is obtained from solve the field in the second derivative equation:

$$\begin{aligned} H_\mathrm{n}^{\parallel} =& \frac{2Dq}{\mu_0 M_\mathrm{s}} - \frac{2Aq^2}{\mu_0 M_\mathrm{s}} + \frac{K_\perp}{\mu_0 M_\mathrm{s}}\left(1+\mathrm{sinc}(qL_y)\cos 2\psi\right) \\ & -\frac{M_\mathrm{s}(1-e^{-qd})}{2qd}(1+\mathrm{sinc}(qL_y)\cos 2\psi). \end{aligned} \tag{2.25}$$

For textures with the pitch vector perpendicular to the applied field, the nucleation field reads

$$\begin{aligned} H_\mathrm{n}^{\perp} =& \frac{2Dq}{\mu_0 M_\mathrm{s}} - \frac{2Aq^2}{\mu_0 M_\mathrm{s}} + \frac{K_\perp}{\mu_0 M_\mathrm{s}}\left(1+\mathrm{sinc}(qL_x)\cos 2\psi\right) \\ & + M_\mathrm{s}\left(\frac{e^{-qd}}{qd}-\frac{1}{qd}+\frac{1}{2}\right)\mathrm{sinc}(qL_x)\cos 2\psi - \frac{M_\mathrm{s}}{2}. \end{aligned} \tag{2.26}$$

In both cases, parallel (bulk-like) and perpendicular (interfacial-like), the nucleation field depends on the strength of the DMI (D), the exchange stiffness (A), the perpendicular anisotropy constant ($K_\perp$), and the pitch vector magnitude (q).

For the symmetry class C_n, the nucleation field depends on the competition of two Dzyaloshinskii-Moriya constants D_1 and D_2:

$$\begin{aligned} \mu_0 H_\mathrm{n}^{C_n} =& \frac{2q\tilde{D}}{M_\mathrm{s}} - \frac{2Aq^2}{M_\mathrm{s}} + \frac{K_\perp}{M_\mathrm{s}}\left(1+\mathrm{sinc}\left(q_x L_x\right)\mathrm{sinc}\left(q_y L_y\right)\cos 2\psi\right) \\ & - \frac{\mu_0 M_\mathrm{s}}{2qd}(e^{-qd}+qd-1)\left[1-\mathrm{sinc}(q_x L_x)\mathrm{sinc}(q_y L_y)\cos 2\psi\right] \\ & - \frac{\mu_0 M_\mathrm{s}}{2qd}(1-e^{-qd})\left[1+\mathrm{sinc}(q_x L_x)\mathrm{sinc}(q_y L_y)\cos 2\psi\right] \end{aligned} \tag{2.27}$$

where $\tilde{D} = \sqrt{D_1^2 + D_2^2}$. Using the fact that $\tan\varphi_q = D_1/D_2$, then it is useful to write

$$qD_1/\tilde{D} = q\cos\varphi_q = q_y, \tag{2.28}$$

and

$$qD_2/\tilde{D} = q\sin\varphi_q = q_x. \tag{2.29}$$

As can be seen in the equations of the nucleation field for a magnetic texture equations 2.25, 2.26, and 2.27, depends on the pitch vector magnitude, and as was discussed in

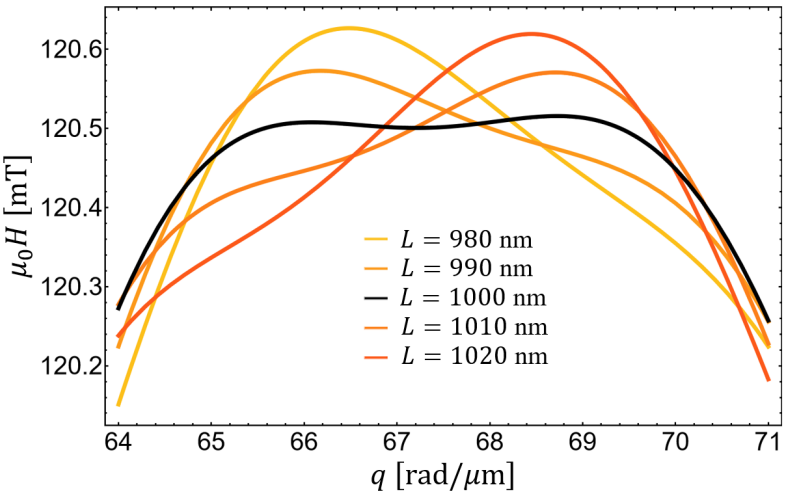

Figure 2.5: Nucleation field strengths plotted as a function of the pitch vector magnitude q for different film sizes. An interfacial DMI strength $D = 1.5$ mJ/m^2 was used. The pitch vector that maximizes the nucleation field is the one that minimizes the micromagnetic energy, as seen in Fig. 2.2(a).

Section 1.4 , just the maximum values of the nucleation field has physical meaning. Then, the value of q that maximizes the nucleation field will be the pitch vector of the conical helix texture that arises when the saturated state becomes unstable [58, 59].

In our previous discussion, we mentioned that the magnitude of the pitch vector depends explicitly on the length of the film. Therefore, the value of q that maximizes the nucleation field varies according to the length L of the film. Fig. 2.5 shows the nucleation field as a function of q for the same film lengths used in Fig. 2.2. Analyzing both figures, it can be verified that the value of q that maximizes the nucleation field coincides with the value of q that minimizes the total energy of the system. This result is consistent since the definition of the effective field can be expressed as $\mathbf{H} = -(1/\mu_0)\delta\varepsilon/\delta\mathbf{M}$. In magnetic systems, different reversal modes can occur, such as conical-helix textures, domain wall motion, curling modes, and coherent rotation. The particular mode that the system selects depends on which mode exhibits the highest nucleation field, in accordance with the discussion presented in Section 1.4. In this context, the history of the magnetization becomes critically important [1]. It should be noted that during transitions between magnetization states, configurations with lower energy than the initial state may exist. However, the fact that a magnetic state has lower energy than the initial state does not necessarily imply that the system will transition to it. For a transition to occur, the selected mode must satisfy the condition of exhibiting the highest nucleation field among the available reversal modes [77–79].
For the C_n symmetry class, the nucleation field is examined in detail. It has two DMI constants, D_1 and D_2. By fixing the value of D_2, a phase diagram can be plotted. Fig. 2.6(a-c) shows the phase diagrams of the magnetic state parametrized by the field strength and D_1 for three specific D_2 magnitudes. Here, the relation between dipolar coupling and superficial anisotropy is given by the quality factor $Q = 1.1$. The states present in the phase diagrams of Fig. 2.6 are the field-polarized state, where the field is sufficiently strong to maintain the magnetization along the applied field, the conical-helix state, and the uniform mode associated either with in-plane or out-of-plane coherent rotation. These two reversal modes are achieved by decreasing the magnetic field from the

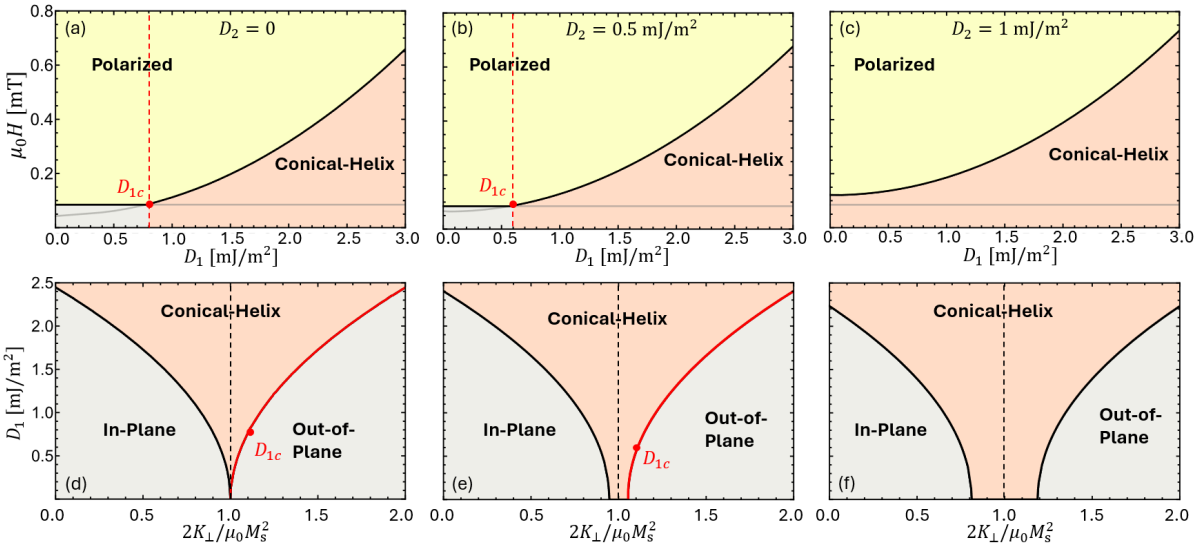

Figure 2.6: Phase diagrams of the magnetic reversal states for the C_n symmetry. The upper-row panels show the magnetic states after a field sweep from a saturating field, as a function of the applied field and DMI constant D_1 for different D_2 constants (in every column) and $Q = 1.1$. A D_{1c} value determines the critical constant D_1, above which the nucleation field for a conical-helix configuration is larger than that of a coherent rotation (given by the horizontal line) ending in an out-of-plane uniform state (square grey region). The lower-row panels show phases of nucleated states (below a nucleation field computed as in the upper-row plots), in the D_1 versus Q landscape, for fixed D_2 constants. The phase regions are delimited by curves of the critical constant D_{1c}.

field-polarized state, where the magnetization will nucleate to either a coherent rotation mode or a conical-helix mode, depending on a critical D_1 value, D_{1c}. For $D < D_{1c}$, the film reverse coherently, either in-plane ($Q < 1$) or out-of-plane ($Q > 1$). Accordingly, nucleated-state phase diagrams as a function of Q and D_1 are depicted in Fig. 2.6(d-f), where, above a critical value, a conical-helix texture is nucleated after field sweep from a saturating field.
From Fig 2.6(d-f), it is observed that increasing the D_2 constant a gap arise around $Q = 1$, which allows tuning the region of conical-helix formation, this means that for C_n symmetry, the transition to a coherent state is not always possible.

2.6 Boundary conditions

The analytical model presented in Eq. 2.1 neglects boundary effects that may result from the exchange, anisotropy, and DM interactions. In this section, we explicitly compute the boundary conditions associated with the interfacial DMI, for the C_{2v} symmetry class, by performing a variational analysis of the energy functional. This procedure naturally reveals the explicit form of the surface terms that must be satisfied at the boundaries of the magnetic film, which are shown in the simulations.
First, we consider the DM energy as a functional of the normalized magnetization vector field, $\mathbf{m}$. For the C_{2v} symmetry, the DM energy functional is given by:

$$E_{\mathrm{dm}}[\mathbf{m}] = \frac{D}{M_s^2} \int_V \left(\mathcal{L}_{xz}^x + \mathcal{L}_{yz}^y \right) \, dV, \tag{2.30}$$

expanding the Lifshitz invariants

$$E_{\mathrm{dm}}[\mathbf{m}] = D\int_V \left(m_x \frac{\partial m_z}{\partial x} - m_z \frac{\partial m_x}{\partial x} + m_y \frac{\partial m_z}{\partial y} - m_z \frac{\partial m_y}{\partial y} \right) dV, \tag{2.31}$$

and after some algebra the total energy simplifies as:

$$E_{\mathrm{dm}}[\mathbf{m}] = D\int_V \left(\mathbf{m} \cdot \left(\frac{\partial \mathbf{m}}{\partial y} \times \hat{\mathbf{x}} \right) - \mathbf{m} \cdot \left(\frac{\partial \mathbf{m}}{\partial x} \times \hat{\mathbf{y}} \right) \right). \tag{2.32}$$

Then, we calculated the contribution to the boundary conditions provided by the DMI through the variation of DM energy functional [80]:

$$\delta E_{\mathrm{dm}}[\mathbf{m}, \mathbf{v}] = \lim_{\epsilon \to 0} \frac{E_{\mathrm{dm}}[\mathbf{m} + \epsilon \mathbf{v}] - E_{\mathrm{dm}}[\mathbf{m}]}{\epsilon}, \tag{2.33}$$

For an arbitrary direction $\mathbf{v}$, which is,

$$\begin{aligned} \delta E_{\mathrm{dm}}[\mathbf{m}, \mathbf{v}] = \lim_{\epsilon \to 0} \frac{d}{d\epsilon} \int_V D \Big\{ & (\mathbf{m} + \epsilon \mathbf{v}) \cdot \left(\frac{\partial}{\partial y} (\mathbf{m} + \epsilon \mathbf{v}) \times \hat{\mathbf{x}} \right) \\ & - (\mathbf{m} + \epsilon \mathbf{v}) \cdot \left(\frac{\partial}{\partial x} (\mathbf{m} + \epsilon \mathbf{v}) \times \hat{\mathbf{y}} \right) \Big\} dV, \end{aligned} \tag{2.34}$$

interchange the derivative with the integral, we solve the derivative and evaluate the limit $\epsilon \to 0$:

$$\begin{aligned} \delta E_{\mathrm{dm}}[\mathbf{m}] = \int_V D \Big\{ & \mathbf{m} \cdot \left(\frac{\partial \mathbf{v}}{\partial y} \times \hat{\mathbf{x}} \right) + \mathbf{v} \cdot \left(\frac{\partial \mathbf{m}}{\partial y} \times \hat{\mathbf{x}} \right) \\ & - \mathbf{m} \cdot \left(\frac{\partial \mathbf{v}}{\partial x} \times \hat{\mathbf{y}} \right) - \mathbf{v} \cdot \left(\frac{\partial \mathbf{m}}{\partial y} \times \hat{\mathbf{x}} \right) \Big\} dV, \end{aligned} \tag{2.35}$$

regrouping

$$\delta E_{\mathrm{dm}}[\mathbf{m}] = \int_V D \Big\{ \mathbf{v} \cdot \left(\frac{\partial \mathbf{m}}{\partial y} \times \hat{\mathbf{x}} - \frac{\partial \mathbf{m}}{\partial x} \times \hat{\mathbf{y}} \right) + \mathbf{m} \cdot \left(\frac{\partial \mathbf{v}}{\partial y} \times \hat{\mathbf{x}} - \frac{\partial \mathbf{v}}{\partial x} \times \hat{\mathbf{y}} \right). \tag{2.36}$$

We notice that

$$\frac{\partial}{\partial x}(\mathbf{m} \cdot (\mathbf{v} \times \hat{\mathbf{y}})) = \frac{\partial \mathbf{m}}{\partial x} \cdot (\mathbf{v} \times \hat{\mathbf{y}}) + \mathbf{m} \cdot \left(\frac{\partial \mathbf{v}}{\partial x} \times \hat{\mathbf{y}} \right), \tag{2.37}$$

$$\mathbf{m} \cdot \left(\frac{\partial \mathbf{v}}{\partial x} \times \hat{\mathbf{y}} \right) = \frac{\partial}{\partial x}(\mathbf{m} \cdot (\mathbf{v} \times \hat{\mathbf{y}})) - \frac{\partial \mathbf{m}}{\partial x} \cdot (\mathbf{v} \times \hat{\mathbf{y}}), \tag{2.38}$$

$$\mathbf{m} \cdot \left(\frac{\partial \mathbf{v}}{\partial x} \times \hat{\mathbf{y}} \right) = \frac{\partial}{\partial x}(\mathbf{m} \cdot (\mathbf{v} \times \hat{\mathbf{y}})) + \mathbf{v} \cdot (\frac{\partial \mathbf{m}}{\partial x} \times \hat{\mathbf{y}}). \tag{2.39}$$

Then we rewrite the second term of the equation (2.36)

$$\begin{aligned} \delta E_{\mathrm{dm}}[\mathbf{m}] = & \int_V 2D \left\{ \mathbf{v} \cdot \left(\frac{\partial \mathbf{m}}{\partial y} \times \hat{\mathbf{x}} - \frac{\partial \mathbf{m}}{\partial x} \times \hat{\mathbf{y}} \right) \right\} dV \\ & + \int_V D \left\{ \frac{\partial}{\partial y}(\mathbf{m} \cdot (\mathbf{v} \times \hat{\mathbf{x}})) - \frac{\partial}{\partial x}(\mathbf{m} \cdot (\mathbf{v} \times \hat{\mathbf{y}})) \right\} dV, \end{aligned} \tag{2.40}$$

interchanging the vector functions in dot and cross product of the second term with the identity: $\mathbf{a}\cdot(\mathbf{b}\times\mathbf{c}) = \mathbf{c}\cdot(\mathbf{a}\times\mathbf{b}) = -\mathbf{c}\cdot(\mathbf{b}\times\mathbf{a})$,

$$\begin{aligned}\delta E_{\mathrm{dm}}[\mathbf{m}] = \int_V 2D\left\{\mathbf{v}\cdot\left(\frac{\partial\mathbf{m}}{\partial y}\times\hat{\mathbf{x}} - \frac{\partial\mathbf{m}}{\partial x}\times\hat{\mathbf{y}}\right)\right\} \\ + \int_V D\left\{\frac{\partial}{\partial x}(\mathbf{v}\cdot(\mathbf{m}\times\hat{\mathbf{y}})) - \frac{\partial}{\partial y}(\mathbf{v}\cdot(\mathbf{m}\times\hat{\mathbf{x}}))\right\}\, dV,\end{aligned} \tag{2.41}$$

using the divergence theorem for the second term, obtain:

$$\begin{aligned}\delta E_{\mathrm{dm}}[\mathbf{m}] = \int_V 2D\left\{\mathbf{v}\cdot\left(\frac{\partial\mathbf{m}}{\partial y}\times\hat{\mathbf{x}} - \frac{\partial\mathbf{m}}{\partial x}\times\hat{\mathbf{y}}\right)\right\} \\ + \int_{\partial\Omega} D\mathbf{v}\cdot\{(\mathbf{m}\times\hat{\mathbf{y}})(\hat{\mathbf{x}}\cdot\hat{\mathbf{n}}) - (\mathbf{m}\cdot\hat{\mathbf{x}})(\hat{\mathbf{y}}\cdot\hat{\mathbf{n}})\}\, dS.\end{aligned} \tag{2.42}$$

Where the first term is $\delta E/\delta\mathbf{m}$, and the second term is $\mathbf{v}\cdot\mathbf{G}$. Where $\mathbf{G}$ is the boundary term associated with the DMI. Then, the boundary condition is write as

$$2A\frac{\partial\mathbf{m}}{\partial n} - \mathbf{G} = 0, \tag{2.43}$$

with

$$\mathbf{G} = D[(\mathbf{m}\times\hat{\mathbf{y}})(\hat{\mathbf{x}}\cdot\hat{\mathbf{n}}) - (\mathbf{m}\cdot\hat{\mathbf{x}})(\hat{\mathbf{y}}\cdot\hat{\mathbf{n}})]. \tag{2.44}$$

The boundary conditions for every studied symmetry class are calculated and shown in the fifth column in table 2.1.
This boundary condition (Eq. 2.43) is not fulfilled by the proposed model in Eq. 2.1, although the calculation of this boundary term helps to understand the behavior of the magnetization at the edges of the film. If we define a magnetization

$$\mathbf{m} = (\sin\theta(\mathbf{r})\sin\psi(\mathbf{r}), \cos\theta(\mathbf{r}), \sin\theta(\mathbf{r})\cos\psi(\mathbf{r}))$$

in the case of C_{nv} symmetry the boundary condition impose:

$$\left.\frac{\partial\psi}{\partial x}\right|_{x=L_x/2} = \frac{D}{2A} \qquad \left.\frac{\partial\theta}{\partial x}\right|_{x=L_x/2} = 0 \tag{2.45}$$

Conclusion

In the present thesis, the conical-helix magnetic textures in thin ferromagnetic films with different kinds of asymmetric exchange, i.e., Dzyaloshinskii-Moriya interactions, have been described by defining a suitable magnetization ansatz. This model contains a series of parameters, including the phase angle, the helix pitch vector, and the cone angle, that can be determined by minimizing the micromagnetic energy functional for the ultrathin planar geometry considered here. Moreover, this technique enables the calculation of a nucleation field of a conical-helix texture when decreasing an applied magnetic field after saturating the sample.

The method employed in this study has been applied to ferromagnetic systems with different crystalline symmetry classes, which are described by DMI energy densities given by different combinations of Lifshitz invariants. This analysis allowed the comparison of the helix parameters obtained from theory and simulation for all these symmetry classes. Moreover, the model fully considers the effect of dipolar interactions in the thin film regime, providing an accurate description of these nonlocal interactions that are usually nontrivial to formulate mathematically. Therefore, the developed formalism serves as a solid foundation for the micromagnetic modeling of helical spin textures in materials with any DMI, or antisymmetric exchange-like interactions, in thin films. This first approach to study helical modulations in confined systems could be of interest for more complex states like syrmion lattices, and hedgehog lattices. Since can be described by three or more helical modulations [20, 21, 81]

The theoretical model was validated against micromagnetic simulations using the novel finite difference code mumax$^+$ and the well-established code OOMMF, to support the results. Although the analytical model does not consider finite-size effects from the sample boundaries, it considers a phase angle due to the finite film since translation symmetry is broken. This phase angle reveals the competition between the dipolar coupling and the perpendicular surface anisotropy and directs the magnetization towards different orientations.

A discontinuous behavior of the pitch vector was found from its minimization together with the wavelength as a function of the length L of the film. Due to the boundaries of the finite film, the dipolar coupling seeks to close magnetic fields line by selecting a half-integer number of helical wavelengths for the magnetic texture, causing an antiparallel magnetization at the edges of the thin film and reducing the total energy. Moreover, based on the nucleation field calculations, the transition states for the C_n symmetry has been analyzed, showing that the conical-helix texture dominates over other competing magnetization textures.

These results show excellent agreement between the analytical solutions and numerical calculations, even without accounting for the finite-size effects at the sample boundaries. To further improve the model, introducing a spatial dependence of the conical angle could be a promising approach. This dependence could be defined for each symmetry class based on the boundary conditions derived in the variational analysis.

Appendix A

Energy terms

A.1 Exchange energy

The energy associated with the intralayer exchange coupling is given by:

$$E_{\text{ex}} = \int_V \frac{A}{M_{\text{s}}^2} \left[\left(\nabla^2 M_x\right)^2 + \left(\nabla^2 M_y\right)^2 + \left(\nabla^2 M_z\right)^2 \right] \, dV. \tag{A.1}$$

Inserting the model for the magnetization, 2.1, the exchange energy density is:

$$\varepsilon_{\text{ex}} = \frac{Aq^2}{\mu_0 M_{\text{s}}^2} \sin^2\theta. \tag{A.2}$$

A.2 Zeeman energy

The energy associated to the Zeeman energy is:

$$E_{\text{Z}} = -\mu_0 \int_V \mathbf{M} \cdot \mathbf{H} \, dV \tag{A.3}$$

Then, the density energy is:

$$\varepsilon_{\text{Z}} = -\frac{H \cos\theta}{M_{\text{s}}} \tag{A.4}$$

A.3 Perpendicular magnetic anisotropy energy

The energy associated to the perpendicular magnetic anisotropy energy is obtained as:

$$E_{\text{s}} = -\frac{K_\perp}{2} \int_V (\mathbf{m} \cdot \hat{\mathbf{z}}) \, dV. \tag{A.5}$$

Then the density energy is:

$$\varepsilon_{\text{s}} = -\frac{K_\perp \sin^2\theta}{2\mu_0 M\text{s}^2} \left[1 + \ \text{sinc}(qL_y \cos\varphi_q) \ \text{sinc}(qL_x \sin\varphi_q) \cos 2\psi\right]. \tag{A.6}$$

For symmetries in which the pitch vector is aligned parallel to the applied field, the anisotropy energy density simplifies to:

$$\varepsilon_{\text{s}}^{\parallel} = -\frac{K_\perp \sin^2\theta}{2\mu_0 M\text{s}^2} \left[1 + \text{sinc}(qL_y) \cos 2\psi\right]. \tag{A.7}$$

For symmetries where the pitch vector is oriented perpendicular to the applied field, the anisotropy energy density becomes:

$$\varepsilon_{\mathrm{s}}^{\perp} = -\frac{K_{\perp}\sin^2\theta}{2\mu_0 M\mathrm{s}^2}\left[1+\mathrm{sinc}(qL_x)\cos 2\psi\right] \tag{A.8}$$

Finally, for the crystallographic point group C_{n}, the surface anisotropy energy density takes the form:

$$\varepsilon_{\mathrm{s}}^{\mathrm{Cn}} = -\frac{K_{\perp}\sin^2\theta}{2\mu_0 M\mathrm{s}^2}\left[1+\ \mathrm{sinc}\left(\frac{D_1}{\tilde{D}}qLx\right)\ \mathrm{sinc}\left(\frac{D_2}{\tilde{D}}qLy\right)\cos 2\psi\right] \tag{A.9}$$

A.4 Dipolar coupling

As it was discussed in section 1.1.2, the magnetic scalar potential is calculated to obtain the dipolar coupling,

$$\nabla^2 U(\mathbf{r}) = \nabla\cdot\mathbf{M}(\mathbf{r}), \tag{A.10}$$

inserting the model from equation (2.1) into the right-hand side of equation (A.10), yields

$$\nabla\cdot\mathbf{M}(\mathbf{r}) = M_{\mathrm{s}}q\cos(qy\cos\varphi_q + qx\sin\varphi_q+\psi)\sin\theta\sin\varphi_q \tag{A.11}$$

A particular solution for the magnetic scalar potential has provide in [58, 82]

$$U(\mathbf{r}) = \begin{cases} a\sin\theta\cos(\mathbf{q}\cdot\mathbf{r}+\psi)e^{-qz} & ,z>d/2,\\ (Ae^{-qz}+Be^{qz})\sin\theta\cos(\mathbf{q}\cdot\mathbf{r}+\psi)-\frac{\nabla\cdot\mathbf{M}(\mathbf{r})}{q^2} & ,-d/2\le z\le d/2,\\ b\sin\theta\cos(\mathbf{q}\cdot\mathbf{r}+\psi)e^{qz} & ,z<-d/2 \end{cases} \tag{A.12}$$

Then the coefficients are obtain from the boundary condition along z. See equations 1.9, 1.10.

$$a = A+Be^{qd}-\frac{M_{\mathrm{s}}e^{qd/2}\sin\varphi_q}{q} \tag{A.13}$$

$$b = Ae^{qd}+B-\frac{M_{\mathrm{s}}e^{qd/2}\sin\varphi_q}{q} \tag{A.14}$$

$$A = -\frac{M_{\mathrm{s}}(1-\sin\varphi_q)e^{-qd/2}}{2q} \tag{A.15}$$

$$B = \frac{M_{\mathrm{s}}(1+\sin\varphi_q)e^{-qd/2}}{2q} \tag{A.16}$$

$$\tag{A.17}$$

The magnetic scalar potential inside the film is:

$$U(\mathbf{r}) = \frac{M_{\mathrm{s}}}{2q}\sin\theta\sin\varphi_q\cos(\mathbf{q}\cdot\mathbf{r}+\psi)e^{-q(d/2+z)}\left(e^{2qz}-1+\sin\varphi_q\left(1+e^{-2qz}-2e^{-q(d/2-z)}\right)\right). \tag{A.18}$$

Now, the dipolar field is obtained from $\mathbf{H}=\nabla\mathbf{U}(\mathbf{r})$, and the dipolar energy can be obtain from equation 1.11, thus the normalized energy is:

$$\begin{aligned}\varepsilon_{\mathrm{dip}} = \frac{\sin\theta}{4qd}\Big[&\left(qd+e^{-qd}-1\right)\sin\theta\sin^2\varphi_q\left(1-\mathrm{sinc}(q_xL_x)\ \mathrm{sinc}(q_yL_y)\cos 2\psi\right)\\ &+4\left(qd+e^{-qd}-1\right)\cos\theta\sin\psi\sin^2\varphi_q\ \mathrm{sinc}(q_xL_y)\ \mathrm{sinc}(q_yL_y)\\ &+\sin\theta(1-e^{-qd})(1+\mathrm{sinc}(q_xL_x)\ \mathrm{sinc}(q_yL_y)\cos 2\psi)\Big]\end{aligned} \tag{A.19}$$

For the symmetries with the texture parallel to the applied field, $q_x = 0$ and $q_y = q$, the dipolar density energy yields to:

$$\varepsilon_{\text{dip}}^{\parallel} = \frac{\sin^2\theta}{4qd}(1 - e^{-qd})(1 + \text{sinc}(qL_y)\cos 2\psi). \tag{A.20}$$

And for the symmetries with the texture perpendicular to the applied field, $q_x = q$ and $q_y = 0$, the dipolar density energy yields:

$$\begin{aligned}\varepsilon_{\text{dip}}^{\perp} = \frac{\sin\theta}{4qd}\Big[&\left(qd + e^{-qd} - 1\right)\sin\theta\,(1 - \text{sinc}(qL_x)\cos 2\psi) \\ &+4\left(qd + e^{-qd} - 1\right)\cos\theta\sin\psi\ \text{sinc}(qL_x) \\ &+(1 - e^{-qd})\sin\theta(1 + \text{sinc}(qL_x)\cos 2\psi)\Big]\end{aligned} \tag{A.21}$$

Bibliography

[1] A. Aharoni, *Introduction to the Theory of Ferromagnetism* (Oxford University Press, 2000).

[2] J. M. D. Coey, *Magnetism and magnetic materials* (Cambridge university press, 2010).

[3] A. Hubert and R. Schäfer, *Magnetic domains: the analysis of magnetic microstructures* (Springer Science & Business Media, 2008).

[4] A. G. Gurevich and G. A. Melkov, *Magnetization Oscillations and Waves* (CRC Press, Inc, 1996).

[5] P. Landeros and A. S. Núñez, J. Appl. Phys. **108**, 033917 (2010).

[6] D. D. Sheka, O. V. Pylypovskyi, P. Landeros, Y. Gaididei, A. Kákay, and D. Makarov, Commun. Phys. **3**, 128 (2020).

[7] G. Carbou, Math. Models Methods Appl. Sci. **11**, 1529 (2001).

[8] R. V. Kohn and V. V. Slastikov, Arch. Ration. Mech. Anal. **178**, 227 (2005).

[9] J. Lindner and M. Farle, in *Magnetic Heterostructures: Advances and Perspectives in Spinstructures and Spintransport* (Springer, 2008) pp. 45–96.

[10] C. Kittel and P. McEuen, *Introduction to solid state physics* (John Wiley & Sons, 2018).

[11] B. Dieny and M. Chshiev, Rev. Mod. Phys. **89**, 025008 (2017).

[12] I. Dzyaloshinsky, Journal of Physics and Chemistry of Solids **4**, 241 (1958).

[13] T. Moriya, Phys. Rev. Lett. **4**, 228 (1960).

[14] P. W. Anderson, Physical Review **115**, 2 (1959).

[15] I. Dzyaloshinskii, Sov. Phys. JETP **20**, 223 (1965).

[16] A. N. Bogdanov and D. A. Yablonskii, Sov. Phys. JETP **68**, 101 (1989).

[17] D. Cortés-Ortuño and P. Landeros, J. Phys: Cond. Matt. **25**, 156001 (2013).

[18] I. A. Ado, A. Qaiumzadeh, A. Brataas, and M. Titov, Phys. Rev. B **101**, 161403 (2020).

[19] N. Nagaosa and Y. Tokura, Nat. Nanotech. **8**, 899 (2013).

[20] S. Mühlbauer, B. Binz, F. Jonietz, C. Pfleiderer, A. Rosch, A. Neubauer, R. Georgii, and P. Böni, Science **323**, 915 (2009).

[21] Y. Fujishiro, N. Kanazawa, T. Nakajima, X. Z. Yu, K. Ohishi, Y. Kawamura, K. Kakurai, T. Arima, H. Mitamura, A. Miyake, K. Akiba, M. Tokunaga, A. Matsuo, K. Kindo, T. Koretsune, R. Arita, and Y. Tokura, Nature Communications **10**, 1059 (2019).

[22] M. Soda, E. M. Forgan, E. Blackburn, E. Campillo, V. Ryukhtin, I. Hoffmann, A. Kikkawa, Y. Taguchi, H. Yoshizawa, and H. Kawano-Furukawa, Nature Physics **19**, 1476 (2023).

[23] B. Lebech, J. Bernhard, and T. Freltoft, Journal of Physics: Condensed Matter **1**, 6105 (1989).

[24] M. Uchida, N. Nagaosa, J. He, Y. Kaneko, S. Iguchi, Y. Matsui, and Y. Tokura, Physical Review B—Condensed Matter and Materials Physics **77**, 184402 (2008).

[25] H. Wilhelm, M. Baenitz, M. Schmidt, U. Rößler, A. Leonov, and A. Bogdanov, Physical review letters **107**, 127203 (2011).

[26] J. Beille, J. Voiron, and M. Roth, Solid state communications **47**, 399 (1983).

[27] K. Ishimoto, Y. Yamaguchi, J. Suzuki, M. Arai, M. Furusaka, and Y. Endoh, Physica B: Condensed Matter **213**, 381 (1995).

[28] A. Fert, in *Metallic Multilayers*, Materials Science Forum, Vol. 59 (Trans Tech Publications Ltd, 1991) pp. 439–480.

[29] R. A. Gallardo, D. Cortés-Ortuño, R. E. Troncoso, and P. Landeros, "Three-dimensional magnonics: layered, micro-and nanostructures," (Jenny Stanford Publishing, Berlin, Heidelberg, 2019) pp. 121–160.

[30] M. Kuepferling, A. Casiraghi, G. Soares, G. Durin, F. Garcia-Sanchez, L. Chen, C. H. Back, C. H. Marrows, S. Tacchi, and G. Carlotti, Rev. Mod. Phys. **95**, 015003 (2023).

[31] J. Jena, B. Göbel, V. Kumar, I. Mertig, C. Felser, and S. Parkin, Science Advances **6**, eabc0723 (2020), https://www.science.org/doi/pdf/10.1126/sciadv.abc0723 .

[32] H. Yu, J. Xiao, and H. Schultheiss, Phys. Rep. **905**, 1 (2021).

[33] A. Fert, N. Reyren, and V. Cros, Nature Reviews Materials **2**, 17031 (2017).

[34] G. Finocchio, F. Büttner, R. Tomasello, M. Carpentieri, and M. Kläui, Journal of Physics D: Applied Physics **49**, 423001 (2016).

[35] B. Göbel, I. Mertig, and O. A. Tretiakov, Physics Reports **895**, 1 (2021), beyond skyrmions: Review and perspectives of alternative magnetic quasiparticles.

[36] M. Uchida, Y. Onose, Y. Matsui, and Y. Tokura, Science **311**, 359 (2006).

[37] N. Ogawa, L. Köhler, M. Garst, S. Toyoda, S. Seki, and Y. Tokura, PNAS **118**, e2022927118 (2021).

[38] S. Seki, M. Garst, J. Waizner, R. Takagi, N. D. Khanh, Y. Okamura, K. Kondou, F. Kagawa, Y. Otani, and Y. Tokura, Nat. Commun. **11**, 256 (2020).

[39] Y. Ishikawa, K. Tajima, D. Bloch, and M. Roth, Solid State Commun. **19**, 525 (1976).

[40] K. Motoya, H. Yasuoka, Y. Nakamura, and J. Wernick, Solid State Commun. **19**, 529 (1976).

[41] Y. Ishikawa, G. Shirane, J. A. Tarvin, and M. Kohgi, Phys. Rev. B **16**, 4956 (1977).

[42] P. Bak and M. H. Jensen, J. Phys. C: Solid State Phys. **13**, L881 (1980).

[43] T. Moriya and T. Miyadai, Solid State Commun. **42**, 209 (1982).

[44] K. Ishimoto, Y. Yamaguchi, S. Mitsuda, M. Ishida, and Y. Endoh, J. Magn. Magn. Mater. **54-57**, 1003 (1986).

[45] M. Bode, M. Heide, K. von Bergmann, P. Ferriani, S. Heinze, G. Bihlmayer, A. Kubetzka, O. Pietzsch, S. Blügel, and R. Wiesendanger, Nature **447**, 190 (2007).

[46] X. Z. Yu, Y. Onose, N. Kanazawa, J. H. Park, J. H. Han, Y. Matsui, N. Nagaosa, and Y. Tokura, Nature **465**, 901 (2010).

[47] S. Demokritov and A. Slavin, *Magnonics: From Fundamentals to Applications*, Topics in Applied Physics (Springer Berlin Heidelberg, 2012).

[48] G. Gubbiotti (Ed.), "Three-dimensional magnonics: layered, micro-and nanostructures," (Jenny Stanford Publishing, 2019).

[49] S. M. Rezende, *Fundamentals of magnonics*, Vol. 969 (Springer, 2020).

[50] A. Barman, G. Gubbiotti, S. Ladak, A. O. Adeyeye, M. Krawczyk, J. Gräfe, C. Adelmann, S. Cotofana, A. Naeemi, V. I. Vasyuchka, B. Hillebrands, S. A. Nikitov, H. Yu, D. Grundler, A. V. Sadovnikov, A. A. Grachev, S. E. Sheshukova, J.-Y. Duquesne, M. Marangolo, G. Csaba, W. Porod, V. E. Demidov, S. Urazhdin, S. O. Demokritov, E. Albisetti, D. Petti, R. Bertacco, H. Schultheiss, V. V. Kruglyak, V. D. Poimanov, S. Sahoo, J. Sinha, H. Yang, M. Münzenberg, T. Moriyama, S. Mizukami, P. Landeros, R. A. Gallardo, G. Carlotti, J.-V. Kim, R. L. Stamps, R. E. Camley, B. Rana, Y. Otani, W. Yu, T. Yu, G. E. W. Bauer, C. Back, G. S. Uhrig, O. V. Dobrovolskiy, B. Budinska, H. Qin, S. van Dijken, A. V. Chumak, A. Khitun, D. E. Nikonov, I. A. Young, B. W. Zingsem, and M. Winklhofer, J. Phys. Condens. Matter **33**, 413001 (2021).

[51] D. Petti, S. Tacchi, and E. Albisetti, Journal of Physics D: Applied Physics **55**, 293003 (2022).

[52] B. Flebus, D. Grundler, B. Rana, Y. Otani, I. Barsukov, A. Barman, G. Gubbiotti, P. Landeros, J. Akerman, U. Ebels, P. Pirro, V. E. Demidov, K. Schultheiss, G. Csaba, Q. Wang, F. Ciubotaru, D. E. Nikonov, P. Che, R. Hertel, T. Ono, D. Afanasiev, J. Mentink, T. Rasing, B. Hillebrands, S. V. Kusminskiy, W. Zhang, C. R. Du, A. Finco, T. van der Sar, Y. K. Luo, Y. Shiota, J. Sklenar, T. Yu, and J. Rao, J. Phys. Condens. Matter **36**, 363501 (2024).

[53] K. Zakeri, Y. Zhang, J. Prokop, T.-H. Chuang, N. Sakr, W. X. Tang, and J. Kirschner, Phys. Rev. Lett. **104**, 137203 (2010).

[54] R. L. Melcher, Phys. Rev. Lett. **30**, 125–128 (1973).

[55] M. Kataoka, J. Phys. Soc. Jpn. **56**, 3635 (1987).

[56] L. Udvardi and L. Szunyogh, Phys. Rev. Lett. **102**, 207204 (2009).

[57] A. T. Costa, R. B. Muniz, S. Lounis, A. B. Klautau, and D. L. Mills, Phys. Rev. B **82**, 014428 (2010).

[58] C. Ríos-Venegas, F. Brevis, R. A. Gallardo, and P. Landeros, Phys. Rev. B **105**, 224403 (2022).

[59] J. Kisielewski, P. Gruszecki, M. Krawczyk, V. Zablotskii, and A. Maziewski, Phys. Rev. B **107**, 134416 (2023).

[60] M. Janoschek, F. Bernlochner, S. Dunsiger, C. Pfleiderer, P. Böni, B. Roessli, P. Link, and A. Rosch, Phys. Rev. B **81**, 214436 (2010).

[61] M. Kugler, G. Brandl, J. Waizner, M. Janoschek, R. Georgii, A. Bauer, K. Seemann, A. Rosch, C. Pfleiderer, P. Böni, and M. Garst, Phys. Rev. Lett. **115**, 097203 (2015).

[62] T. Schwarze, J. Waizner, M. Garst, A. Bauer, I. Stasinopoulos, H. Berger, C. Pfleiderer, and D. Grundler, Nat. Mater. **14**, 478 EP (2015).

[63] M. Weiler, A. Aqeel, M. Mostovoy, A. Leonov, S. Geprägs, R. Gross, H. Huebl, T. T. M. Palstra, and S. T. B. Goennenwein, Phys. Rev. Lett. **119**, 237204 (2017).

[64] M. Garst, J. Waizner, and D. Grundler, Journal of Physics D: Applied Physics **50**, 293002 (2017).

[65] M. Cepeda-Arancibia, F. Brevis, S. J. R. Holt, D. Cortés-Ortuño, H. Fangohr, and P. Landeros, "Conical-helix magnetic textures stabilized in thin films with different kinds of dzyaloshinskii-moriya interaction," (2025).

[66] S. Rohart and A. Thiaville, Phys. Rev. B **88**, 184422 (2013).

[67] A. O. Leonov, T. L. Monchesky, N. Romming, A. Kubetzka, A. N. Bogdanov, and R. Wiesendanger, New J. Phys. **18**, 065003 (2016).

[68] J. Rowland, S. Banerjee, and M. Randeria, Phys. Rev. B **93**, 020404 (2016).

[69] A. K. Nayak, V. Kumar, T. Ma, P. Werner, E. Pippel, R. Sahoo, F. Damay, U. K. Rößler, C. Felser, and S. S. P. Parkin, Nature **548**, 561 (2017).

[70] J. Jena, B. Göbel, T. Ma, V. Kumar, R. Saha, I. Mertig, C. Felser, and S. S. Parkin, Nature communications **11**, 1115 (2020).

[71] F. N. Rybakov, A. B. Borisov, S. Blügel, and N. S. Kiselev, New Journal of Physics **18**, 045002 (2016).

[72] M. Hoffmann, B. Zimmermann, G. P. Müller, D. Schürhoff, N. S. Kiselev, C. Melcher, and S. Blügel, Nature Communications **8**, 308 (2017).

[73] L. Moreels, I. Lateur, D. D. Gusem, J. Mulkers, J. Maes, M. V. Milosevic, J. Leliaert, and B. V. Waeyenberge, "mumax+: extensible gpu-accelerated micromagnetics and beyond," (2024), arXiv:2411.18194 [cond-mat.mes-hall] .

[74] M. Donahue and D. Porter, *OOMMF User's Guide, Version 2.1a0*, Gaithersburg, MD (2023).

[75] M. Beg, M. Lang, and H. Fangohr, IEEE Trans. Magn. **58**, 1 (2022).

[76] H. Fangohr, M. Lang, S. J. R. Holt, S. A. Pathak, K. Zulfiqar, and M. Beg, AIP Adv. **14**, 015138 (2024).

[77] G. Leaf, H. Kaper, M. Yan, V. Novosad, P. Vavassori, R. E. Camley, and M. Grimsditch, Phys. Rev. Lett. **96**, 017201 (2006).

[78] F. Montoncello, L. Giovannini, F. Nizzoli, P. Vavassori, M. Grimsditch, T. Ono, G. Gubbiotti, S. Tacchi, and G. Carlotti, Phys. Rev. B **76**, 024426 (2007).

[79] F. Montoncello, L. Giovannini, B. Farmer, and L. De Long, Journal of Magnetism and Magnetic Materials **423**, 158 (2017).

[80] C. Abert, The European Physical Journal B **92**, 1 (2019).

[81] R. Takagi, J. S. White, S. Hayami, R. Arita, D. Honecker, H. M. Rønnow, Y. Tokura, and S. Seki, Science Advances **4**, eaau3402 (2018).

[82] R. Arias and D. L. Mills, Phys. Rev. B **60**, 7395 (1999).